JOURNAL OF GEOPHYSICAL RESEARCH, VOL. 103, NO. A10, PAGES 23,485–23,501, OCTOBER 1, 1998

Inner magnetospheric superthermal electron transport: Photoelectron and plasma sheet electron sources

G. V. Khazanov,[1] M. W. Liemohn,[2] J. U. Kozyra,[3] and T. E. Moore[4]

Abstract. Two time-dependent kinetic models of superthermal electron transport are combined to conduct global calculations of the nonthermal electron distribution function throughout the inner magnetosphere. It is shown that the energy range of validity for this combined model extends down to the superthermal-thermal intersection at a few eV, allowing for the calculation of the entire distribution function and thus an accurate heating rate to the thermal plasma. Because of the linearity of the formulas, the source terms are separated to calculate the distributions from the various populations, namely photoelectrons (PEs) and plasma sheet electrons (PSEs). These distributions are discussed in detail, examining the processes responsible for their formation in the various regions of the inner magnetosphere. It is shown that convection, corotation, and Coulomb collisions are the dominant processes in the formation of the PE distribution function and that PSEs are dominated by the interplay between the drift terms. Of note is that the PEs propagate around the nightside in a narrow channel at the edge of the plasmasphere as Coulomb collisions reduce the fluxes inside of this and convection compresses the flux tubes inward. These distributions are then recombined to show the development of the total superthermal electron distribution function in the inner magnetosphere and their influence on the thermal plasma. PEs usually dominate the dayside heating, with integral energy fluxes to the ionosphere reaching 10^{10} eV cm^{-2} s^{-1} in the plasmasphere, while heating from the PSEs typically does not exceed 10^{8} eV cm^{-2} s^{-1}. On the nightside, the inner plasmasphere is usually unheated by superthermal electrons. A feature of these combined spectra is that the distribution often has upward slopes with energy, particularly at the crossover from PE to PSE dominance, indicating that instabilities are possible.

1. Introduction

A distinctive feature of inner magnetospheric plasma is the presence of nonthermal electrons in the energy range of several eV to several keV. This electron population is formed in the ionosphere as a result of ionization of the atmospheric neutral atoms and molecules by photoionization or impact ionization and also convects in from the tail through the plasma sheet. These superthermal electrons play a very important role in a large number of ionospheric and plasmaspheric processes.

Superthermal electrons created in the lower ionosphere (below about 250 km) deposit their energy before they have a chance to move out of this region. This is due to the high density of neutral particles reducing the mean free path. Inelastic scattering processes, combined with the source spectrum, determine the fine structure of the electron distribution function. The distribution is also fairly isotropic. In this region, a local equilibrium approximation (which omits transport) with discrete energy loss is valid [e.g., *Victor et al.*, 1976; *Jasperse*, 1976].

In the upper ionosphere, however, transport processes become more important. A portion of the superthermal electrons generated in this region can escape from the atmosphere and travel out along magnetic field lines. Collisions are still very important in determining the structure of the distribution function, with a transition from discrete to continuous (i.e., Coulomb collisions) energy-loss mechanisms dominating the energy deposition of the superthermal electrons. Transport models that include several pitch angle grid points, such as the two-stream and multi-stream approaches, have been extensively used [e.g., *Banks and Nagy*, 1970; *Mantas and Bowhill*, 1975; *Polyakov et al.*, 1976; *Strickland et al.*, 1976; *Prather et al.*, 1978; *Stamnes*, 1980; *Khazanov and Gefan*, 1982; *Porter et al.*, 1987; *Lummerzheim et al.*, 1989; *Link*, 1992], as well as Monte Carlo particle tracking methods [e.g., *Berger et al.*, 1970; *Cicerone and Bowhill*, 1971; *Solomon*, 1993].

An important aspect of ionospheric source superthermal electrons is their transport through the magnetosphere, particularly photoelectrons (PEs) along low latitude to midlatitude field lines through the plasmasphere. Since Coulomb collisions of superthermal electrons with thermal electrons and ions are rare in this region, it was thought that PEs pass through the plasmasphere to the conjugate ionosphere unhindered. In this case, the plasmasphere is transparent and can be removed from the calculation. However, discrepancies were noticed between observations and this assumption [*Galperin and Mulyarchik*, 1966; *Peterson et al.*, 1977], and it was realized that scattering processes are sufficiently important to be

[1]Geophysical Institute and the Department of Physics, University of Alaska Fairbanks.
[2]Space Sciences Laboratory, NASA Marhsall Space Flight Center, Huntsville, Alabama.
[3]Space Physics Research Laboratory, University of Michigan, Ann Arbor.
[4]Laboratory for Extraterrestrial Physics, NASA Goddard Space Flight Center, Greenbelt, Maryland.

Paper number 98JA02291.
0148-0227/98/98JA-02291$09.00

included in the calculation. The small-angle scattering of the PEs in the plasmasphere can change the motion of the electrons enough to trap some of them in the plasmasphere. This trapping is caused by the magnetic bottle set up by the inhomogeneous magnetic field strength along the flux tube. Initial calculations were qualitative and focused on the thermal plasma heating due to this plasmaspheric scattering [*Sanatani and Hanson*, 1970; *Nagy and Banks*, 1970], and later studies calculated the differential transparency of the plasmasphere [*Takahashi*, 1973; *Swartz et al.*, 1975; *Lejeune and Wörmser*, 1976; *Khazanov et al.*, 1979b]. The PE distribution function in the plasmasphere was eventually calculated [*Mantas et al.*, 1978; *Lejeune*, 1979; *Polyakov et al.*, 1979; *Khazanov et al.*, 1992], but these were steady state calculations based on separate treatments of the ionosphere and plasmasphere. A spatially self-consistent but time-independent calculation was conducted by *Khazanov et al.* [1994], extending the results of *Khazanov et al.* [1992]. *Khazanov et al.* [1993] presented a time-dependent plasmaspheric calculation, investigating the refilling and depletion rates of the PEs in the trapped zone. This model was then extended to include the ionospheres at each end of the field line for the first non steady state, spatially self-consistent calculation of PEs [*Khazanov and Liemohn*, 1995].

One process, however, that was not included in the study by *Khazanov and Liemohn* [1995] is magnetospheric convection. It was assumed that the flux tube was corotating with the Earth, so that cross field line drift effects could be neglected. Recently, simulations on a global scale have been carried out showing the influence of these cross field drift effects on the development of the high-energy PE distribution function [*Khazanov et al.*, 1996]. This study showed that this population requires many hours to reach a steady state level in the magnetosphere.

Another source of superthermal electrons in the inner magnetosphere is the plasma sheet. Because of the sunward flow of plasma from the dawn-to-dusk electric field in the magnetosphere, plasma sheet electrons (PSEs) and ions are continually pushed toward the Earth, regulated by geomagnetic activity. *Alfvén and Fälthammar* [1963] calculated drift patterns for these particles, showing the classic tear-drop boundary between closed and open trajectories (that is, trajectories that return to their starting point and those that do not). This separatrix is often called the Alfvén boundary, and while the magnetosphere is never constant enough for the steady-state assumption of this boundary to be valid, it is a very powerful tool for qualitatively describing the shape and motion of particles in near-Earth space. The motion of the PSEs in from the tail, around this boundary, and out on the dayside is well known and regularly observed at geosynchronous orbit [e.g., *DeForest and McIlwain*, 1971; *Eather et al.*, 1976; *Hultqvist et al.*, 1981; *Arnoldy*, 1986; *McComas et al.*, 1993; *Birn et al.*, 1997]. Enhancements in geomagnetic activity cause this boundary to move in closer to the Earth, and there have been numerous observational and theoretical studies on the motion of electrons in this injection front toward the Earth near local midnight [e.g., *Roederer*, 1970; *Barfield et al.*, 1977; *Ejiri*, 1978; *Ejiri et al.*, 1978, 1980; *Kaye and Kivelson*, 1979; *Moore et al.*, 1981; *Moore and Arnoldy*, 1982; *Arnoldy and Moore*, 1983; *Kerns et al.*, 1994; *Burke et al.*, 1995; *Liemohn et al.*, 1998]. A typical approach to modeling this population is to average the distribution function along the field line (with appropriate mapping to conserve the first adiabatic invariant), which is valid if the bounce period is much shorter than any drift or collisional timescale. This assumption is usually true for electrons greater than a few tens of electron volts. While the injected PSE distribution is usually isotropic (*Birn et al.* [1997] found that the $T_\perp/T_\parallel$ ratio for PSEs at geosynchronous is usually between 1.0 and 1.3), it has sometimes been noted that the pitch angle distribution of sub-keV electrons in the injection front form a possible source cone distribution, and that high-energy electrons can have a peak at 40° pitch angle or less [*Moore and Arnoldy*, 1982; *Koons and Fennell*, 1983; *Arnoldy*, 1986]. A strong increase in the intensity of the low-energy fluxes during injections has also been observed [*Ejiri et al.*, 1980]. One observation of injected PSEs showed the formation of a banded energy structure in the captured electrons [*Burke et al.*, 1995]. This event was simulated with a time-dependent, bounce-averaged model by *Liemohn et al.* [1998], determining that the bands in energy are a natural consequence of captured electrons due to the supercorotation of high-energy electrons caused by magnetic gradient-curvature drift. The bands only formed when the injected PSEs were contained inside the Alfvén boundary for a prolonged period. The increase in intensity in the sub-keV energy range was also shown to be a natural occurrence of the relaxation of the flux tubes on the nightside.

The theoretical studies of this nonthermal electron population in the inner magnetosphere have so far not addressed the combination of the sources described above. The present study provides a quantitative description of superthermal electron distribution function formation on a global scale in the presence of both PE and PSE source populations for various geomagnetic conditions. In particular, the extension of the bounce-averaged energy range down to several electron volts is examined, allowing for an accurate comparison of not only the relative intensities but also the energy deposition to the thermal plasma for the two populations. The observations of captured PSEs by CRRES [*Burke et al.*, 1995] will also be further examined with this combined distribution function.

2. Model Description

The model for this study to calculate the superthermal electron distribution function in the ionosphere-plasmasphere system is based on coupling two of our existing models: our field-aligned and bounce-averaged transport codes. These two models complement each other and for the first time offer a unique possibility for simulating superthermal electron motion on a global scale.

2.1. Configuration of the Field-Aligned and Bounce-Averaged Models

The first model simulates superthermal electron transport through a flux tube in the geomagnetic field. It calculates the time-dependent superthermal electron distribution function, f, as a function of time, distance along the field line, energy, and pitch angle from the gyration-averaged kinetic equation [*Khazanov and Liemohn*, 1995; *Liemohn et al.*, 1997a]:

$$\frac{\beta}{\sqrt{E}}\frac{\partial\phi}{\partial t}+\mu\frac{\partial\phi}{\partial s}-\frac{1-\mu^2}{2}\left(\frac{1}{B}\frac{\partial B}{\partial s}-\frac{F}{E}\right)\frac{\partial\phi}{\partial\mu}+EF\mu\frac{\partial}{\partial E}\left(\frac{\phi}{E}\right)=Q+\bar{S} \quad (1)$$

where $\phi=2Ef/m^2$ is the superthermal electron flux; $\beta=(2/m)^{1/2}=1.7\times10^{-8}$ eV$^{1/2}$s/cm; t is time; s is the distance

along the field line; E is the particle energy; and μ is the cosine of the pitch angle. The inhomogeneity of the geomagnetic field, B, is included, as well as other forces, such as electric fields, in F. Q is the superthermal electron source term and $\bar{S}$ includes the collision integrals, representing interactions with thermal electrons and ions, scattering with neutral particles, and wave-particle interactions.

Initially, this model was developed for transport in the plasmasphere to investigate the refilling and depletion timescales of the trapped zone [*Khazanov et al.*, 1993], with boundary fluxes needed at the ionospheric interfaces. The ionospheres were then incorporated [*Khazanov and Liemohn*, 1995, 1998; *Liemohn and Khazanov*, 1995], including elastic and inelastic collisions with neutral particles, for a spatially self-consistent calculation along a flux tube. In these studies, the concept of plasmaspheric transparency was addressed, showing that this quantity is highly energy dependent and that a unified approach is needed. Recently, it was coupled with the time-dependent, field-aligned, hydrodynamic thermal plasma model of *Guiter et al.* [1995] to determine the coupling effects between these populations [*Liemohn et al.*, 1997a, *Liemohn and Khazanov*, 1998], particularly the influence of a self-consistent field-aligned electric field.

The second model of superthermal electron transport calculates the distribution on a global scale throughout the subauroral magnetosphere. When the flight time along the magnetic field line, τ_b, is very short compared to the collisional timescales, it is possible to average the particle fluxes along the field line over a magnetic mirror bounce period. By including particle drifts across field lines, superthermal electron fluxes for the entire inner magnetosphere can be determined by solving the bounce-averaged kinetic equation [*Khazanov et al.*, 1996] :

$$\frac{\partial\langle f\rangle}{\partial t}+\langle \mathbf{V}_D\rangle\frac{\partial\langle f\rangle}{\partial \mathbf{R}_\perp}+\left\langle\frac{dE}{dt}\right\rangle\frac{\partial\langle f\rangle}{\partial E}+\left\langle\frac{d\mu_0}{dt}\right\rangle\frac{\partial\langle f\rangle}{\partial \mu_0}=\left\langle\frac{\delta f}{\delta t}\right\rangle-\frac{2\langle f\rangle}{\tau_b} \quad (2)$$

where $\mathbf{R}_\perp$ includes the spatial directions R and φ perpendicular to the magnetic field and $\mathbf{V}_D$ is the drift velocity in these coordinates, μ_0 is the cosine of the pitch angle at the magnetic equator, and $\langle\xi\rangle$ denotes averaging ξ over a bounce period along the field line. The spatial extent of this model encircles the globe at radial distances from L=1.75 out to L=6.5, providing a complimentary solution of the kinetic equation to the first model throughout the subauroral magnetosphere. Currently, the only collisional process is Coulomb interactions with the thermal plasma, and atmospheric precipitation is treated as a loss.

This model has been used for PE and PSE applications. The formation of the high-energy PE distribution ($E\geq$50 eV) was examined with this model [*Khazanov et al.*, 1996], showing that cross-field convection is an important process, particularly the transport of electrons through the nightside into the dawn sector. This model has also been used to investigate the formation of the banded electron structure observed by *Burke et al.* [1995] as PSEs were injected into the inner magnetosphere [*Liemohn et al.*, 1998]. That study focused on the capture of the electron cloud and the formation of the bands; this study will proceed a step further and examine the contribution of PEs to the observed distributions.

2.2. Combined Global Model

As was mentioned above, the simulation of the superthermal electron population is based on two major source regions: the ionosphere (PEs and the secondary electrons produced by them) and the magnetotail (PSEs). Because the PEs are generated in the atmosphere, their plasmaspheric velocity space distribution has a source cone at pitch angles that map to the ionospheres. The PE trapped population is built up by scattering these electrons while they are in the plasmasphere. The timescale for the formation of the distribution function in the source cone is much faster than that for the trapped zone because the former is controlled by field-aligned transport and the latter by diffusion [*Khazanov et al.*, 1993; *Liemohn et al.*, 1997a]. It was also shown by *Khazanov et al.* [1996] that cross-field drift effects are significant to the development of this trapped zone population. Because of these vastly different timescales, it is possible to separate the solution into two components: (1) a field-aligned calculation to determine the source function and the plasmaspheric source cone distribution and (2) a bounce-averaged calculation for the trapped zone.

The PSE calculation can also be separated into these two components. As the plasma convects around the nightside, it moves closer to the Earth, experiencing a stronger magnetic field where a greater amount of the pitch angle domain is connected to the ionosphere. This part of velocity space is a loss cone, and particles will undergo severe energy loss upon entering the upper atmosphere. This loss process is much faster than the convection or scattering of particles into the fly-through zone, and so the calculation can be divided as above: a bounce-averaged calculation for the development of the trapped zone fluxes and a field-aligned calculation for the loss cone and ionospheric regions, including the production of secondary electrons.

This study combines these two separate calculations into a single consistent approach. The two models described above present a unique possibility in modeling the non steady state development of the superthermal electron distribution function, providing complementary calculations for a feedback loop of loss cone-trapped zone distribution functions. The field-aligned model is used to calculate the PE distribution function in the plasmaspheric source cone, and these results are used as a boundary condition on the dayside in the bounce-averaged model. This allows for the calculation of the initial PE source terms in the ionosphere and their self-consistent propagation between the conjugate footpoints through the inner magnetosphere with the first model, and then using these flux intensities in the second model to simulate the cross-field drift effects on the PE distribution function. It also allows for the calculation of the PE influence to the nightside plasmasphere.

Conversely, the bounce-averaged model can be used to calculate a boundary condition for the field-aligned model. Here precipitation effects of superthermal electrons can be investigated, including thermal plasma heating and secondary production in the ionosphere. These field-aligned model results of backscattering and secondary electron production can then be incorporated back into the bounce-averaged model to calculate the cross-field drift of these electrons.

Khazanov et al. [1992] discussed an analytical approach to self-consistently coupling the superthermal electron solutions in the loss cone and in the trapped zone. In that study, a boundary flux injected into the plasmasphere from the topside ionosphere determined the distribution in the fly-through zone using a field-aligned transport equation, and a bounce-averaged kinetic equation was used in the trapped zone. The solutions of these two equations were matched at the pitch angle of the loss cone-trapped zone boundary. This solution was used to calcu-

late the transparency of the plasmasphere for the superthermal electrons and from this the heating rates to the thermal plasma. These results, however, are dependent on the functional form of the assumed distribution at the ionospheric boundary. The model in the present study avoids this restriction because it contains a unified approach to the spatial regions by coupling the field-aligned and the bounce-averaged transport models. Also, this combined model is time dependent, so the development of the distribution function can be examined.

2.3. Numerical Implementation

Each code maintains its own numerical implementation because the only interface is the exchange of results at appropriate times. Below is a brief outline of the modeling procedure for each approach, which involves discretizing the derivatives on a phase space grid and solving for f. A comprehensive description has been given previously for both the field-aligned model [*Khazanov et al.*, 1994; *Khazanov and Liemohn*, 1995; *Liemohn et al.*, 1997a] and for the bounce-averaged model [*Fok et al.*, 1993; *Jordanova et al.*, 1996; *Khazanov et al.*, 1996].

The field-aligned code includes the calculation of the distribution in the magnetosphere, where pitch-angle diffusion is the dominant process for scattering particles in to and out of the trapped zone. Therefore the numerical scheme of this model is a second-order pitch angle diffusion scheme at each point in time, energy, and distance, with fully implicit differences for the derivatives in these three variables. In order to decrease undesirable computational effects associated with approximation errors of the derivatives $\partial/\partial s$ and $\partial/\partial\mu$, it is convenient to change variables from (μ, s) to (μ_0, s) [*Khazanov et al.*, 1979b, 1994], where $\mu_0=(1-(1-\mu^2)B_0/B)^{1/2}$ Because μ_0 comes from the first adiabatic invariant, ϕ is now a slowly varying function with s [*Khazanov et al.*, 1993]. The pitch angle grid is nonuniform, allowing more grid points near the edge of the loss cone where the distribution function rapidly changes, typically with 100 grid points per directional hemisphere. These grid points are added as the magnetic field decreases, starting with 5 to 10 in the low-altitude ionosphere and building up to resolve the distribution in the geomagnetic trap. *Liemohn and Khazanov* [1995] presented a calculation of energy conservation and numerical diffusion for this model, finding that the energy conservation is within the expected numerical error (1-10%, depending on grid spacing, when calculated to steady state).

The bounce-averaged global model uses a combination of second-order high-resolution methods for the advection operators and a second-order diffusion scheme for pitch angle scattering. The time step here must be chosen small enough to satisfy the Courant-Fredricks-Lewy condition at each phase space point, $|v_{CFL}|\le|a(R,\varphi,E,\mu_0,t)\Delta t/\Delta x|\le 1$, where Δx is the local step in variable x (R, φ, E, or μ_0) and a is the corresponding velocity. The time step is therefore usually less than 10 s for superthermal electron simulations, and Δt=5 s was used throughout these runs. This code was recently modified for parallel computing efficiency, with a speed up of well over an order of magnitude compared to its performance on a workstation [*McGuire and Liemohn*, 1997]. The numerical diffusion and dispersion of this technique has been discussed by *Leveque* [1992] and *Fok* [1993], with much less than 1% error in the results (when calculated to steady state).

The field-aligned and bounce-averaged model use the same energy grid. For this study, it is a geometrically increasing energy step to provide a smooth transition from low to high energies. This also allows for many points at low-energies to capture the fine structure in this region, while simultaneously supplying a reasonable number of grid points at high energies. The number of energy steps ranged from 65 to 75 for the simulations presented below.

The linearized Fokker-Planck collision operator will be used for the Coulomb interactions in (1) and (2) [*Hinton*, 1983, as described by *Khazanov and Liemohn*, 1995]. Because the simulations can be separated out by the source terms, that is, into distinct PE and PSE calculations, results from each population will be individually presented and discussed, followed by a discussion of the combined distribution from both sources. First, however, a critical issue must by addressed: the proper low-energy limit of this model.

3. Low-Energy Limit of the Combined Model

Traditionally, bounce averaging of the kinetic equation is only applicable down to energies with a bounce period much smaller than the collisional timescales, typically above several tens of eV for electrons. However, once a "quasi-steady-state" flux level is achieved in the fly-through zone (see section 3.2), a bounce-averaged approximation can be applied for much lower energies, even for electrons of a few eV energy. Phenomenologically, this extension is justified because of the very different timescales for distribution function development in the loss cone and trapped zone, and separate models are used to calculate the fluxes in these two regions of velocity space.

3.1. Desired Low-Energy Limit

To determine the desired low-energy limit, we will compare the superthermal electron energy spectra with that of a typical thermal electron distribution. Figure 1 shows pitch angle averaged fluxes for these two populations (thermal and nonthermal electrons) at two altitudes along an L=4 field line, in units of $(cm^2\ eV\ s\ sr)^{-1}$. The superthermal spectra is from a typical photoelectron source, and the fluxes have been averaged over pitch angle for comparison with the thermal plasma spectra, which is assumed to be an isotropic Maxwellian, $\phi_{te0}=n_0 E\exp(-E/E_0)/[8\pi^4 mE_0^3]^{1/2}$, where the values of n_0 and

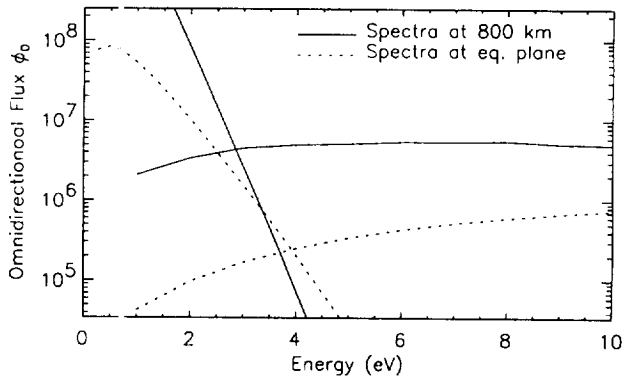

Figure 1. Omnidirectional fluxes for a Maxwellian thermal plasma and modeled photoelectrons at two altitudes along an L=4 flux tube. Thermal plasma parameters are given in Table 1.

Table 1. Determining the Desired Low-Energy Limit

	n cm^{-3}	E_0 K	H_e cm	E_{int} eV	E_b eV
800 km	3.1×10^4	3000	6.9×10^7	2.8	2.3
Eq. plane	360	5000	1.4×10^{10}	3.9	3.7

E_0 are given in Table 1. The intersection energies E_{int} are 2.8 eV at 800 km and 3.9 eV at the top of the field line. Note that the pitch angle averaging includes the trapped zone at the equatorial plane, which is relatively empty compared to the source cone. By definition, there is no trapped zone at 800 km.

Another method of determining the desired lower-energy limit of the superthermal electron energy range is by comparing the transport timescale τ_s to the collisional timescale τ_{ee} (the Maxwellization time). The energy where these two quantities equate, E_b, is where the distribution changes from "thermal" to "nonthermal" because the electrons are collision-dominated below this energy and transport-dominated above it. The timescales can be defined as

$$\tau_s = \frac{H_e}{\bar{v}} = \frac{n_e}{\bar{v}\left|dn_e/ds\right|} \qquad \tau_{ee} = \frac{1}{\bar{v}n_e\sigma_e} = \frac{E^2}{A\bar{v}n_e} \tag{3}$$

where H_e is the scale height of the electron distribution, n_e is the total electron density, and $A=2\pi e^4 \ln\Lambda = 2.6\times10^{-12}$ cm^{2}eV^2. From (3), we get $E_b=(An_eH_e)^{1/2}$. For the same L=4 field line used in Figure 1, E_b is 2.3 eV at 800 km and 3.7 eV at the equatorial plane. The relevant quantities for this calculation are given in Table 1. Knowing this, it is possible to analyze (1) and (2) to determine if the model is valid down to this energy limit. So, both methods reveal approximately the same low energy limit for the superthermal electron energy range.

3.2. Calculation of the Limit

The bounce-averaged approximation can only be used when the distribution is a slowly-varying function of field-aligned distance. During the initial stages of transport through a flux tube, this is clearly not the case, but once this initial front of particles has traversed the flux tube, the variation along the field line is greatly reduced [*Khazanov and Liemohn*, 1995; *Liemohn et al.*, 1997a]. It is in this "quasi-steady-state" limit where transient flows have settled that the validity of (2) will be explored.

The spatial variation of the distribution function along the field line for a given equatorial pitch angle is proportional to the bounce path length for that pitch angle. Therefore, the most field-aligned variation in the trapped zone occurs at its interface with the fly-through zone (α_b). Also, (1) and (2) should yield the same distribution function at α_b because it is shared by both velocity space regions. Note that such a match can only be done if the variation of f_b along the field line is small. Therefore the validity of matching these equations is connected to the applicability of the bounce-averaged equation at the edge of the loss cone and therefore throughout the trapped zone.

As discussed in section 2.2, the fluxes in the fly-through zone reach steady state very quickly after the initial flows have passed because changes in the source are very slow compared to the interhemispherical traversal time. Therefore the time derivatives can be omitted for this analysis and the field-aligned kinetic equation becomes [*Khazanov et al.*, 1993],

$$\mu\frac{\partial f}{\partial s} = \frac{An_e}{E}\frac{\partial f}{\partial E} + \frac{An_e}{2E^2}\frac{B_0}{B_i}\frac{\mu}{\mu_0}\frac{\partial}{\partial\mu_0}\left[\frac{\mu}{\mu_0}\left(1-\mu_0^2\right)\frac{\partial f}{\partial\mu_0}\right] \tag{4}$$

where the subscripts i and 0 refer to the ionosphere-plasmasphere interface (where the loss cone is defined) and the equatorial plane, respectively. Also, the bounce-averaged kinetic equation reduces to [e.g., *Khazanov et al.*, 1992]

$$\frac{\partial}{\partial\mu_0}\left[a(\mu_0)\left(1-\mu_0^2\right)\frac{\partial\langle f\rangle}{\partial\mu_0}\right] + 2b(\mu_0)E\frac{\partial\langle f\rangle}{\partial E} = 0 \tag{5}$$

where a and b are coefficients from the integral over a bounce period. Note that (5) can be derived from (4) if f is a slowly varying function of s [*Khazanov et al.*, 1979a].

Note that while μ changes for a particle trajectory along a field line, it's equatorial value μ_0 is constant (except for changes due to collisional scattering). To combine (4) and (5) into one equation to solve for $f_b(\mu_{0b})$, we can use the fact that the variation near μ_{0b} of $\partial f/\partial\mu_0$ is much bigger than the variation of a or μ/μ_0. So, assuming that at μ_{0b} we can write $\mu/\mu_0\approx d$ and $a(\mu_0)\approx a$, then the pitch angle diffusion terms in (4) and (5) can be matched to yield

$$\mu\frac{\partial f_b}{\partial s} = \frac{An_e}{E}\left[1-\frac{B_0}{B_i}\frac{bd^2}{a}\right]\frac{\partial f_b}{\partial E} \tag{6}$$

Now (6) can be solved for f_b. For the sake of simplicity, the energy variation of f in the low-energy superthermal range will be parameterized as an exponential, $f(E)\propto\exp(-E/E_s)$, and so (6) reduces to an ordinary differential equation resulting in

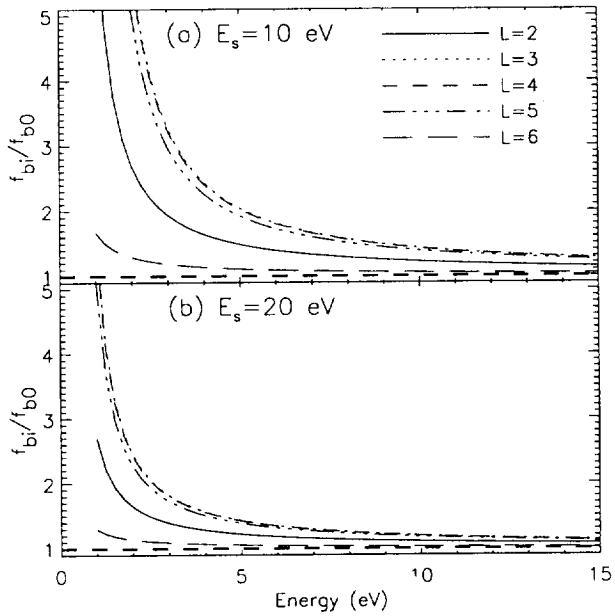

Figure 2. Ratios of topside ionosphere values to magnetic equator values of the electron distribution function at the loss cone-trapped zone boundary at various L shells. Flux ratios are from the solution of (12), with (top) E_s=10 eV (bottom) and 20 eV. The relevant parameters given in Table 2. A heavy dashed line at unity is shown for reference.

Table 2. Loss Cone Boundary f Ratios at 4 eV

L	B_i/B_0	α_{0b} deg	μ_{0b}	n_{e0} cm^{-3}	f_{bi}/f_{b0} E_0=10 eV	f_{bi}/f_{b0} E_0=20 eV
2	8.53	20.0	0.940	2.3×10^3	1.7	1.3
3	32.1	10.2	0.984	1.0×10^3	2.4	1.6
4	79.8	6.4	0.994	360	2.4	1.6
5	160.	4.5	0.997	180	2.3	1.5
6	281.	3.4	0.998	15	1.1	1.1

$$\frac{f_{b,i}}{f_{b,0}} = \exp\left\{-\int_{s_i}^{s_0} \frac{An_e(s')}{\mu(s')EE_s}\left[\frac{B_0}{B_i}\left(\frac{\mu(s')}{\mu_0}\right)^2\frac{b}{a}-1\right]ds'\right\} \quad (7)$$

Plots of (7) are shown in Figure 2 for E_s=10 and 20 eV at several L values. These choices for E_s are typical mean values of superthermal electrons in the low-energy range. The distribution function ratio is the value of f at the loss cone boundary at 800 km to that at the equatorial plane. The thermal plasma densities used are given in Table 2 along with the magnetic field ratio and the equatorial pitch angle of the loss cone-trapped zone boundary α_{0b} (and its cosine, μ_{0b}). Figure 2 shows that the f_b ratios are quite reasonable down to the desired low-energy limit (the 4 eV values listed in Table 2). They are well below the corresponding magnetic field ratios, indicating that the decrease along the field line due to collisions is rather insignificant compared with the changes due to the inhomogeneous magnetic field. Note that the L=3 and L=4 results are on top of each other, and are slightly higher than the L=5 ratios. Numerical results from the field-aligned transport model confirm that $f_b(\mu_{0b})$ converges very quickly, the greatest field-aligned variation in the trapped zone occurs at μ_{0b}, and the code yields very similar flux ratio results for times after the initial front has passed through the plasmasphere. It is clear from this analysis that a bounce-averaged approach is valid down to very low superthermal electron energies, as long as impulsive field-aligned flows are omitted. The L shell dependence of these ratio curves is mainly due to the thermal density.

This extension allows for the calculation of the total energy spectrum of the nonthermal electron population, as well as an accurate determination of the energy deposition rate from the PE and PSE populations to the thermal plasma. These topics will now be addressed.

4. Photoelectron Distribution Function Formation

As discussed above, the linearity of (1) and (2) affirms that the distribution functions from the various source terms can be calculated independently, and then summed at the end to show the combined result. The PE source will be discussed first, followed by the PSE source term.

4.1. Photoelectron Source Spectrum

An important feature of the PE source spectrum is the presence of spikes due to specific emission lines in the solar EUV spectrum. A prominent line is the He II 30.4 nm line. With an energy of 40 eV, this strong line produces a series of peaks in the 20-30 eV electron energy range due to the various ionization states of the atmospheric constituents.

Another important feature of the photoelectron source spectrum is the presence of the Auger electron peaks. This is due to the double ionization of atmospheric particles by high-energy photons. These photons initially produce a free electron from an inner electron shell of the neutral. Then an electron from the outermost shell transitions down to fill the hole, releasing a photon equal to this transition energy. This photon, however, does not escape but instead produces another free electron from the outermost shell. This second electron is known as an Auger electron, and has an energy of 300-500 eV, depending on the particle it originated from. There have been only a few modeling efforts to include this population [*Avakyan et al.*, 1977; *Winningham et al.*, 1989], showing that the inclusion of Auger electrons is necessary to obtain good agreement with observations while maintaining reasonable soft X ray solar fluxes. For the present study, which focuses on the comparison of PE fluxes with PSE fluxes in the inner magnetosphere, Auger electrons are a critical component of the results.

It is useful to compare these model results with data to determine the accuracy of the PE source spectrum to be used in this study. Figure 3 shows such a comparison. Here omnidirectional electron measurements from the Atmospheric Explorer E satellite are plotted along with a model run for the same geophysical conditions. The data were taken on the morningside near the equator on day 355 of 1975 [*Doering et al.*, 1976], at solar zenith angles of 50° and 37° for the two altitudes of 182 km and 365 km, respectively. In Figure 3a, the spectra agree closely for most of the energy range. Figure 3b also shows good agreement, with the model predicting more definition in the 20-30 eV range (from photoionization from the He II 30.4 nm solar line) and slightly lower fluxes above 30 eV. Further comparisons of results from this model with observations are shown by *Khazanov and Liemohn* [1998].

As discussed above, the field-aligned model provides a source term for the bounce-averaged model at the loss cone

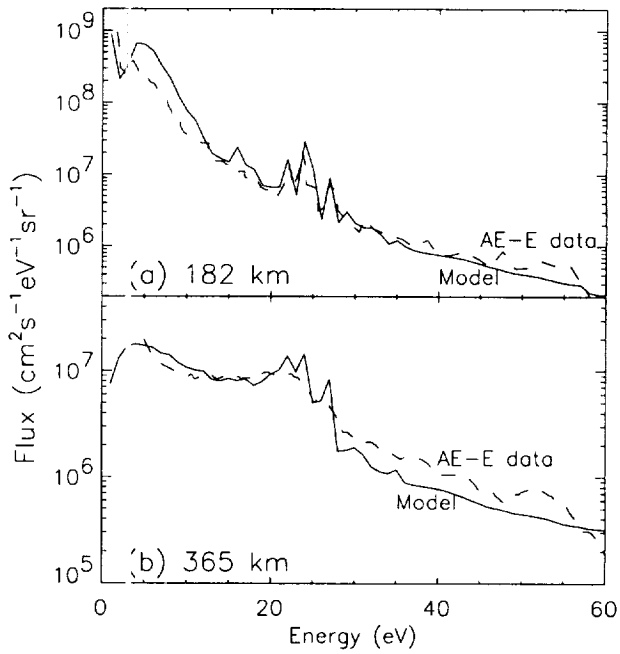

Figure 3. Comparison of model results (solid lines) with AE-E data (dashed lines) at (a) 182 km and (b) 365 km on day 355 of 1975. The satellite data are reproduced from *Doering et al.* [1976].

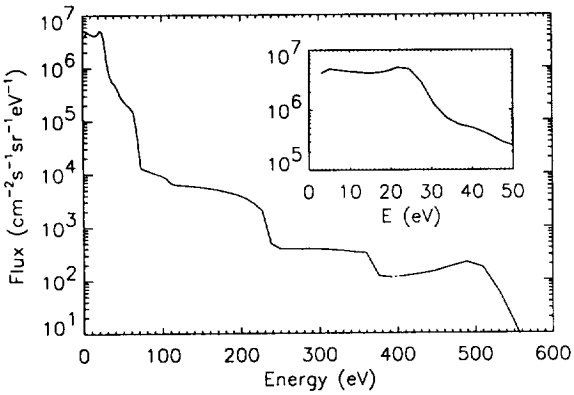

Figure 4. Typical photoelectron spectrum from the field-aligned code used as an input condition for the bounce-averaged model at the loss cone-trapped zone boundary.

boundary on the dayside for the PEs. For the cases to be examined here, a moderately high solar activity level will be used along with various geomagnetic activity levels. The PE source is mostly a function of solar activity level, and largely independent of geomagnetic activity. Therefore the PE source term being supplied to the bounce-averaged model is essentially the same for the various simulations. A typical source cone boundary spectrum is shown in Figure 4. The low-energy range below 5 eV is sloped upward due to Coulomb collisional damping, the production peaks visible in Figure 3 are essentially washed out into a single increase in flux near 25 eV, and the Auger peaks at 360 and 500 eV are quite distinguishable. The production spectrum drops off rapidly above 500 eV because of the absence of the Auger electrons. Note that there is actually fine structure present in the low- and high-energy production peaks resulting from the individual ionization states of the atmospheric constituents, and the resolution of this fine structure is highly dependent on the energy step of the model. The choice of a geometrically increasing energy step for these calculations smoothes out the peaks, especially in the high-energy range. Choosing a ΔE of much less than 1 eV is necessary to accurately resolve each peak [cf. *Jasperse and Smith*, 1978], and the stability of these peaks have been debated as a source of plasma waves [*Butvin et al.*, 1975; *Kudryashev et al.*, 1979; *Ivanov et al.*, 1980, 1982]. Because we are focusing on the global formation and evolution of the distribution function rather than the possible instabilities, a reasonably large energy step was chosen.

4.2. Photoelectrons When $Kp = 1$

A comprehensive calculation of the superthermal electron distribution function throughout the inner magnetosphere from the thermal energy boundary up to tens of keV energies has not been conducted, to our knowledge. The combined model presented above now makes this type of time-dependent, spatially three-dimensional simulation possible for all superthermal electron sources. Because the PE source term is largely independent of geomagnetic activity, a simulation with constant Kp=1 will be discussed in detail, and then other simulations will be compared to these results.

The development of the source cone region of velocity space on the dayside has been shown in previous studies [e.g., *Liemohn and Khazanov*, 1995]. Here we will focus on the formation of the trapped zone flux population. The time development of the 90° pitch angle (equatorially mirroring) energy spectra is shown in Figure 5 for three L values and six magnetic local times. Note the different flux scales for each subplot. Here and throughout the remaining figures, the differential number flux is given in units of (eV cm^2 s sr)$^{-1}$, and the distributions are shown in terms of equatorial pitch angle (these equatorial plane distributions from the bounce-averaged model can easily be mapped along the field line). Because the source is at small pitch angles, the development of the distribution at 90° should be a maximum time scale for PEs. Note the fast buildup of the fluxes on the dayside. A steady state distribution has been reached for most of the PE energy range after 3 hours. This case has relatively high thermal plasma densities, accelerating the scattering of PEs into the trapped zone. On the nightside, the PE fluxes degrade as they move around from dusk to dawn. The peak near 100 eV is due to the source dropping off at higher energies and Coulomb collisions more efficiently absorbing the energy of the slower PEs. The L=5 fluxes are much higher than the L=3 fluxes at MLT=0300. This is not only because of the decreased thermal plasma density at the larger L values but also because of magnetospheric convection compressing the flux tubes from larger L shells. Thus it appears the flux at this L shell remains constant (and even grows) around the nightside. At MLT=0600, this narrow L shell band of PE fluxes contributes to the dayside fluxes in the high-energy trapped zone, creating a bulge in the distribution

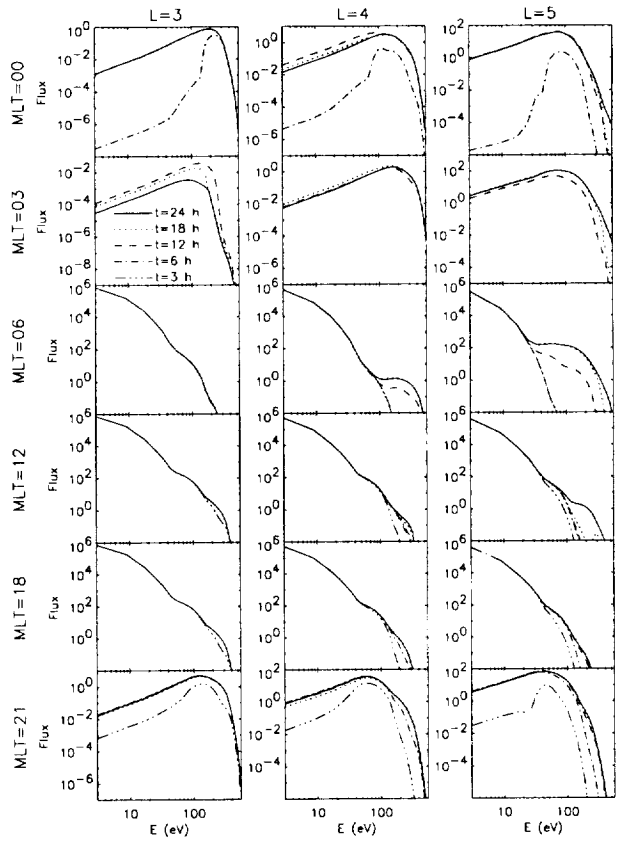

Figure 5. Time development of the 90° equatorial pitch angle energy spectra at various spatial locations in the inner magnetosphere. Simulation times are in hours from photoelectron source turn-on in the dayside ionosphere, with constant Kp=1 geomagnetic activity. Note that each subplot has its own dynamic range. Here and elsewhere, the axis label "flux" refers to differential number flux in (eV cm^2 s sr)$^{-1}$.

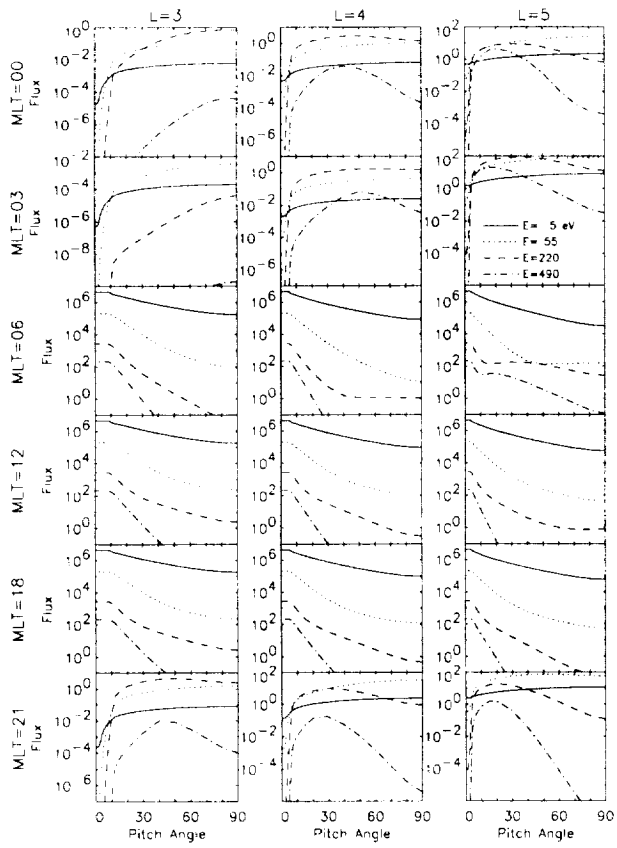

Figure 6. Energy dependence of the steady state equatorial pitch angle distributions at various spatial locations for a photoelectron source with constant Kp=1. Note that each subplot has its own dynamic range.

function. This bulge is seen even at MLT=1200. By 24 hours of simulation time, the fluxes have essentially reached a steady-state level.

The pitch angle distributions at the spatial locations of Figure 5 are shown in Figure 6 for the time-converged results. On the dayside, it is clear that the trapped zone for low-energy electrons is filled in more than the higher energies. On the nightside, the low-energy fluxes are nearly isotropic in the trapped zone. This is not the case at higher energies. In the 220 eV and 490 eV nightside distributions, there is a peak near 30°-40°. This is largely due to Coulomb interactions. At small pitch angles, scattering depletes the loss cone and nearby trapped zone. At large pitch angles, scattering from the source cone on the dayside is not able to fill the loss cone any more than this, because of the competing processes of Coulomb energy decay and spatial drift. Please note that this is different from the source cone distributions observed by *Moore and Arnoldy* [1982], which are due to secondary electrons from precipitating plasma sheet particles, a source not included here. Also, the bulge from the particles convecting through the nightside is clearly seen at MLT=0600, contributing only to the high-energy trapped zone fluxes.

4.3. Analysis of Photoelectron Transport

Figures 5 and 6 presented the development of the PE distribution function for low geomagnetic activity with all drift processes included. It is useful to examine the change in these results under different conditions and with various processes omitted. This will provide insight into why the distribution develops as it does.

First, the influence of the various drift terms will be examined. Using the Volland-Stern convection model [*Volland*, 1973; *Stern*, 1975] and a dipole magnetic field, the bounce-averaged velocity terms in (2) from adiabatic drift can be written in the form [e.g., *Jordanova*, 1995]

$$\left\langle \frac{dR}{dt} \right\rangle = -\frac{AR^4 \cos\varphi}{M_E} \tag{8a}$$

$$\left\langle \frac{d\varphi}{dt} \right\rangle = \frac{C}{M_E} + \frac{AR^3 \sin\varphi}{M_E} - \frac{3ER}{qM_E}\left[1 - \frac{I(\mu_0)}{6h(\mu_0)}\right] \tag{8b}$$

$$\left\langle \frac{dE}{dt} \right\rangle = -\frac{3E}{R}\left[1 - \frac{I(\mu_0)}{6h(\mu_0)}\right]\left\langle \frac{dR}{dt} \right\rangle \tag{8c}$$

$$\left\langle \frac{d\mu_0}{dt} \right\rangle = \frac{\left(1-\mu_0^2\right)}{4R\mu_0}\frac{I(\mu_0)}{h(\mu_0)}\left\langle \frac{dR}{dt} \right\rangle \tag{8d}$$

where R is geocentric distance in the equatorial plane, φ is MLT in radians (φ=0 at MLT=0000), A is a function of geomagnetic activity (Kp in this case, taken from *Maynard and Chen* [1975]), C is a constant characterizing the corotation electric field, M_E=8.02x10^{15} Tm^3 is the magnetic dipole of the Earth, q is the charge of the particle including sign, and $I(\mu_0)$ and $h(\mu_0)$ are slowly varying functions of equatorial pitch angle resulting from the bounce-averaging process [*Ejiri*, 1978]. The various processes can be identified in the right-hand sides of these equations. Corotation yields the first term in (8b); magnetic gradient-curvature drift produces the third term in (8b), and the rest of the terms in (8) are due to magnetospheric convection. By systematically removing these

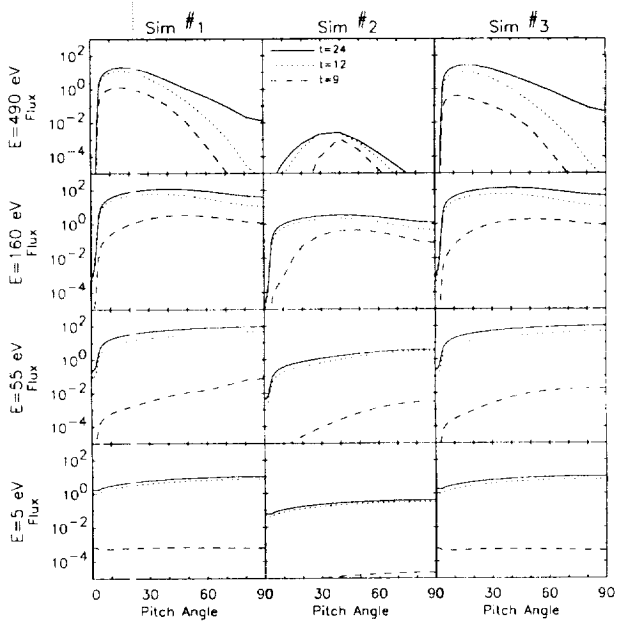

Figure 7. Comparison of the time development of the nightside pitch angle distributions at various energies for three different simulations at MLT=0300, L=5. All three have constant Kp=1, and Sim 1 includes all drift terms, Sim 2 is without magnetospheric convection drift, and Sim 3 is without magnetic gradient-curvature drift.

terms from the calculation, the effects of each drift process can be investigated.

Figure 7 shows a comparison of the pitch angle distributions for three simulations at a nightside spatial location in the PE band (MLT=0300, L=5). All three simulations have a constant Kp=1 with various combinations of the drift terms (listed in Table 3). Sim 1 and 3 look very similar because the energies are too low to be affected by magnetic drifts. Sim 2 is lower than the other two because without magnetospheric convection there is no relaxation on the nightside to enhance the flux at this L shell. These results indicate that it is only the high energy fluxes that benefit the most from this flux tube compression; the low energy region has a large Coulomb loss term that offsets some of the increase. Note that at higher energies, the peak at 30°-40° pitch angles is evident, particularly in the early time results. Its existence in the Sim 2 results suggests that Coulomb collisions are mainly responsible for this peak. Another alternative is the field-aligned acceleration due to the relaxation of the stretched flux tubes (first-order Fermi acceleration). This is perhaps partly responsible, but Coulomb collisions play a much larger role in forming this peak. The 5 eV fluxes are nearly isotropic, even here on the nightside. Note that the dashed line is at 9 h of simulation time, when the PEs should first be reaching this spatial location. However, most of the energy range needs at least another 3 hours to approach a steady-state level (the high-energy range needs much more than this, in fact). This can be explained by the fact that it takes some amount of time to scatter particles into the trapped zone in the afternoon sector (the source region for PEs on the nightside), so 9 hours is premature to expect a complete distribution at this spatial location. Also, the total convection rate is less than the purely corotational convection rate because magnetospheric convection acts to slow the PEs before local midnight (MLT=1800-2400) for a longer interval than it acts to speed them up (MLT=2400-0300).

It is useful to show a comparison of the relative strengths of the azimuthal (MLT) drift terms from (8b). These drifts are shown in Figure 8, in units of hours of magnetic local time per simulation hour. Corotation is at unity and constant with L. The magnetic gradient-curvature drifts are weakly pitch angle and L dependent and strongly energy dependent. Two energy values are shown for a pitch angle of 80°, with the higher one repeated for 20°. From this it is clear that magnetic drifts are unimportant at PE energies, but it will be the dominant drift term at higher energies. Note that due to the negative charge of electrons, this drift is in the same direction as corotation. Drift due to magnetospheric convection is dependent on Kp, and a high and low value are shown. This drift is also dependent on MLT, and so MLT=0600 was chosen to show the maximum positive azimuthal drift due to convection. This φ drift will vanish at MLT=0000 and 1200, and will counteract corotation at MLT=1800. This shows that corotation always dominates convection in the inner part of the spatial domain, but during high activity convection will dominate in the outer part of the spatial domain. This will most likely be true even for a more realistic convection electric field description.

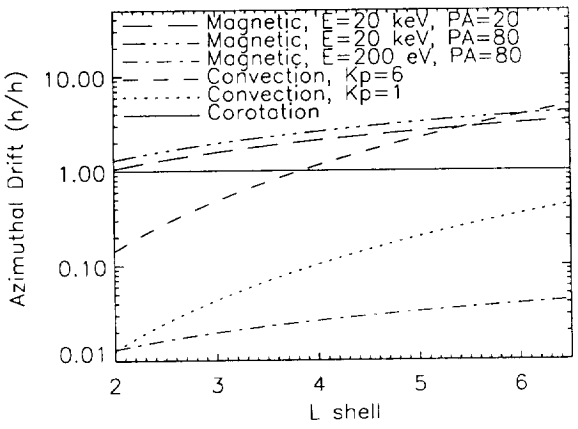

Figure 8. Radial dependence of various azimuthal (MLT) drift terms in hours of magnetic local time per simulation hour. Terms shown are for corotation (solid line), magnetospheric convection at MLT=0600 (where the azimuthal component is greatest) for Kp=1 (dotted line) and Kp=6 (dashed line), and the gradient-curvature effects from the magnetic field for electron energies of 200 eV (dash-dot line) and 20 keV (dash-dot-dot-dot line) for 80° pitch angle and also 20 keV with 20° pitch angle (long dash line).

Table 3. PE Comparison Simulations

Simulation	Kp	Processes
1	1	all included
2	1	no magnetospheric convection
3	1	no gradient-curvature drift
4	1	no drifts at all
5	6	all included

Not shown in Figure 7 are the other two simulations listed in Table 3. This is because the fluxes are zero for these two cases at this spatial location. No PEs should be expected on the nightside when there is no spatial drift, as is the case for Sim 4. When Kp=6 (Sim 5), corotation only dominates very close to the Earth, and so this spatial location is outside of the Alfvén boundary for all PE energies and no PE flux is expected. Also, the corotating region where PEs are expected has a large thermal plasma density, and so the PE fluxes in the nightside plasmasphere are very small.

The effects of these two simulations will make a difference on the dayside, however, and this is shown in Figure 9. Here steady state pitch angle distributions are presented for L=5 at several energies and magnetic local times. Notice that Sim 5 is drastically different from the other results. This is because the enhanced magnetospheric convection pushes the plasma out the dayside boundary before it can build up. Only in the afternoon sector at low energies is there enough time for Coulomb scattering to fill in the trapped zone to a level close to the low geomagnetic activity simulations. Sim 4 and Sim 5 do not show the high-energy bulge on the dawnside because there is no plasma entering from the nightside for these cases. Sim 2 has a much smaller trapped zone bulge intensity than Sim 1, and it does not persist as far into the dayside either. Sim 2 does, however, have a larger flux at high energies in the afternoon sector because there is no magnetospheric convection to strip the plasma away. This is also true for the comparison of Sim 1 and Sim 4 at low energies at dawn. Because MLT=0600 is at the beginning of the PE source region, all azimuthal drifts act to deplete the low-energy trapped zone at this MLT. Thus Sim 4 has slightly higher fluxes at low energies here.

Several conclusions can be made from these comparisons. One is that magnetospheric convection plays a large role in

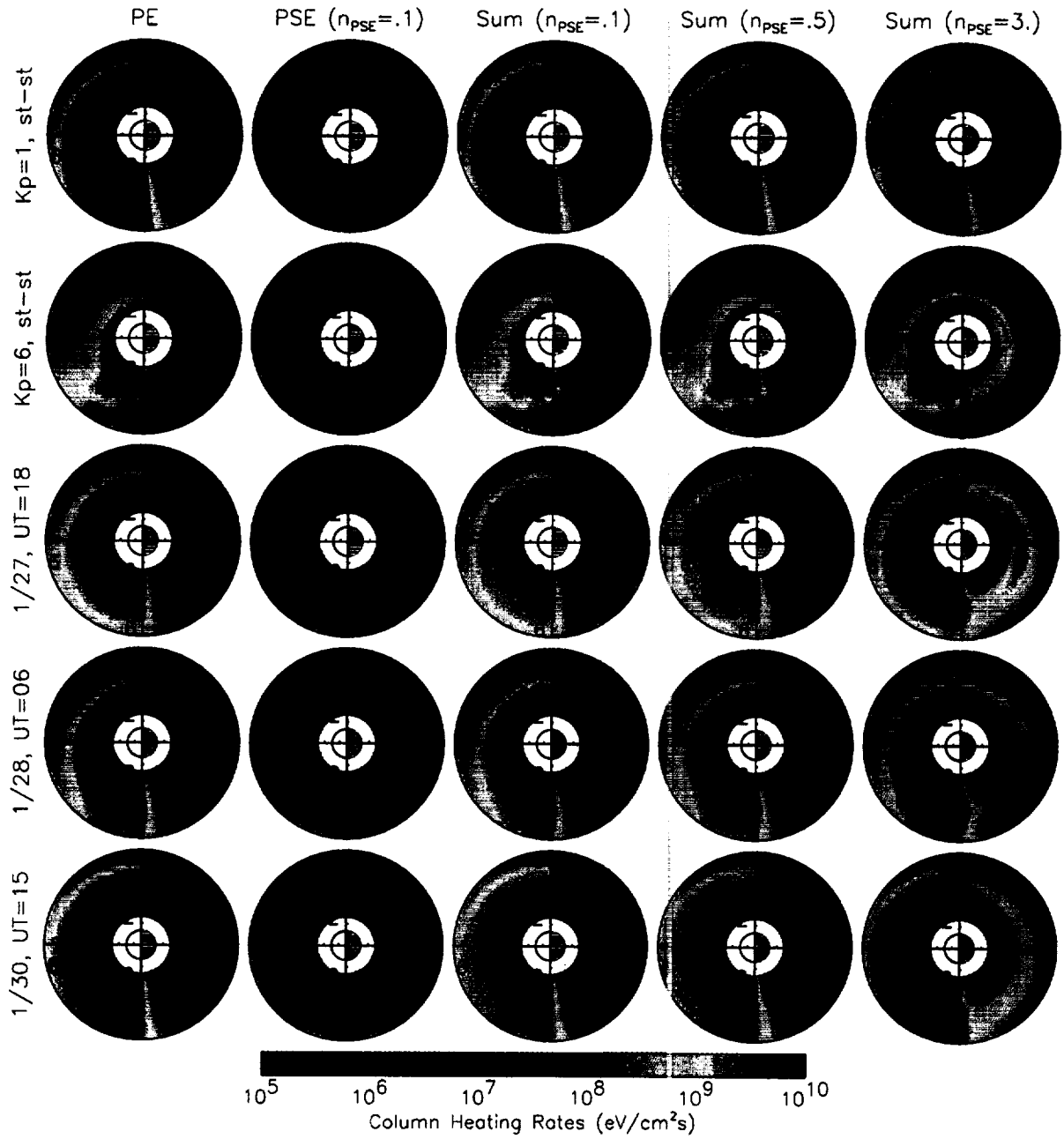

Plate 1. Flux tube-integrated energy deposition rates to the thermal electrons for photoelectrons, plasma sheet electrons, and the combined distribution for three plasma sheet densities. The first row is constant Kp=1 at steady state, the second row is constant Kp=6 at steady state, and the last three rows are at times during late January 1991.

the development of the PE distribution. It creates a high-energy bulge in a narrow L band on the nightside that propagates into the dawn sector, and it acts to deplete the trapped zone fluxes on the dayside by sweeping the plasma away before it can build up. Magnetic gradient curvature drift is not important for PEs, but Coulomb collisions are very important. This interaction fills in the trapped zone, allowing for a PE population on the nightside, and it removes PEs from the inner plasmasphere on the nightside. High geomagnetic activity completely changes the distribution of PEs throughout the inner magnetosphere, preventing them from moving to the nightside and removing them from the dayside as well.

5. Injection of Plasma Sheet Electrons

For PSEs, the various drift terms play an even more important role in the distribution function formation in the inner magnetosphere because of the characteristics of the source population. For this reason, a real Kp history will be used for the baseline case, and then other simulations will be compared with this one to examine the effects of the various processes.

5.1. Plasma Sheet Boundary Conditions

Liemohn et al. [1998] discussed the necessity for careful determination of where the Alfvén boundary lies in relation to

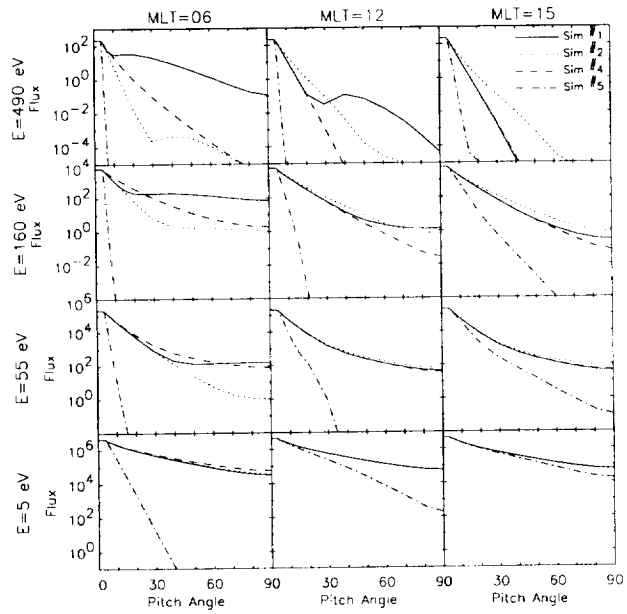

Figure 9. Comparison of the steady-state photoelectron pitch angle distributions at various energies and dayside magnetic local times at L=5 for four different simulations. Sim 1 and Sim 2 are the same as in Figure 9, while Sim 4 has Kp=1 with no drift terms included at all (only collisional processes), and Sim 5 has constant Kp=6 with all processes included.

the outer boundary of the simulation domain. The plasma travels along closed drift paths inside of the Alfvén boundary and along open drift paths outside of it, and this separatrix is highly dependent on geomagnetic activity, as well as energy, pitch angle, and location. The location in φ of where the Alfvén boundary crosses the outer boundary of the simulation at 6.6 R_E, $\varphi_B(E, \mu_o, Kp)$, must be accurately determined, with injected plasma sheet particles entering along the open trajectories (dawnward of φ_B) and corotating plasma distributions from the dayside filling closed trajectories (duskward of φ_B). As in the work of *Liemohn et al.* [1998], φ_B is taken from a look-up table so that the appropriate boundary flux is taken for each energy and pitch angle at each azimuthal angle for each time step.

The models can assume any initial or boundary condition. For the PSEs, the injection flux is assumed to be an isotropic kappa distribution, which resembles a Maxwellian below the characteristic energy E_0 but transitions to a power law of $\phi \propto E^{-\kappa}$ at higher energies. While the injected electrons sometimes have a characteristic energy up to a few keV [*DeForest and McIlwain*, 1971; *Eather et al.*, 1976; *Evans and Moore*, 1979; *Birn et al.*, 1997; *Borovsky et al.*, 1997], *Christon et al.* [1989] found that best fit values for electrons from ISEE 1 measurements during quiet times are κ=6 and E_0=200 eV, and these values will be used in the present study. The density of the injected electrons is taken to be 0.1 cm^{-3} [cf. *Huang and Frank*, 1986; *Baumjohann et al.*, 1989; *Christon et al.*, 1989; *Birn et al.*, 1997]. At the beginning of each simulation (UT=0000 of 1/25/91), it is assumed that there are no PSEs inside of the simulation domain.

The geomagnetic activity level is a critical element in electron transport in the inner magnetosphere. Thus the choice of Kp history is very important. Several simulations will hold the activity level fixed at a low (Kp=1) or high (Kp=6) value, but these are simply illustrative cases. For a realistic simulation, we will use the Kp history of late January 1991. During this time period, the low-energy plasma analyzer (LEPA) instrument on-board the CRRES satellite detected several bands of magnetically trapped 0.1-30 keV electrons inside the plasmapause. *Liemohn et al.* [1998] examined the formation of this banded structure in the inner magnetosphere, concluding that these bands are a natural occurrence when plasma sheet electrons are trapped along closed drift paths in the inner magnetosphere by a sudden decrease of geomagnetic activity. Further simulation results during this time period will be presented, and the possibility of photoelectron additions to the low-energy band of the trapped population causing its mean energy to decrease diabatically (as discussed by *Burke et al.* [1995]) will be investigated. The Kp history for late January 1991 is shown in Figure 10.

Notice in this plot that there are a series of spikes in Kp on top of a relatively low background level. Of interest are the three most prominent spikes at the ends of days 25, 26, and 27. *Burke et al.* [1995] stated that the lowest-energy band was not observed by CRRES until after the last of these spikes. *Liemohn et al.* [1998], however, found that the cloud exists even after the first Kp spike and that the last spike simply adds to the intensity of the cloud. This difference could be from a number of possibilities: the satellite missed the low-energy cloud until the 27th (and thus only measured the high-energy bands elsewhere in space); scattering processes not included in the model rapidly depleted the captured fluxes (such as wave-particle interactions); or the choice of PSE boundary flux is not consistent with the actual injections. *Birn et al.* [1997] showed that both the density and temperature of the electrons during an injection typically rise and then fall off. However, they fitted their distributions with a Maxwellian rather than a kappa distribution, while the changes in temperature are most likely due to enhancements in the tail of the distribution (as seen in their Figure 9). A Maxwellian has a higher characteristic energy than a kappa distribution would need, and thus our choice of boundary condition is not unreasonable. Still, an increase in either κ or E_0 would decrease the number of electrons in the low energy range, and this could explain the absence of the low-energy band in the CRRES observations.

5.2. Plasma Sheet Electrons During the CRRES Observations

Using the Kp history in Figure 10, the PSE injection into the inner magnetosphere can be simulated for the CRRES observations of the banded electron structure event.

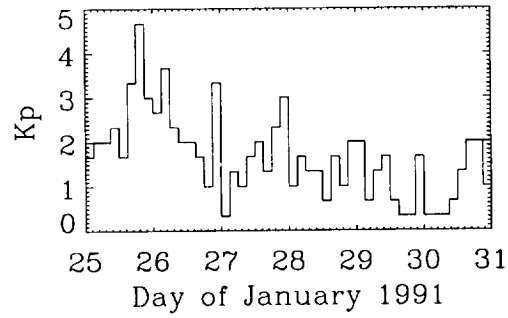

Figure 10. Kp history during the CRRES observations of the banded electron structures.

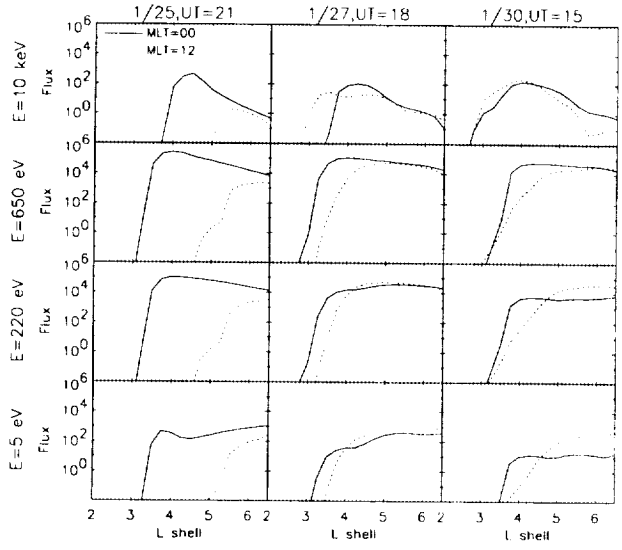

Figure 11. Radial dependence of 90° plasma sheet electrons at various energies and simulation times for late January 1991, shown at local midnight (solid line) and noon (dotted line).

This L shell dependence is shown in Figure 11, illustrating the radial variation of the 90° (equatorially mirroring) flux values at several energies and simulation times. The times shown are during the first and third pulses and then at the end of the simulation, chosen so the peak of the cloud is at local midnight. It is clear that essentially no low-energy PSEs penetrate inside of L=3, but a portion of the high-energy tail of the kappa distribution makes it in this far after the third injection. The 650 eV row shows the fluxes near the peak of the lowest energy band. The degradation of the low-energy fluxes (below 650 eV) due to Coulomb collisions is clearly seen in this figure, although the degradation timescale is slower than for PEs because of the higher mean energies of the PSEs. The high-energy fluxes in the third column look very different from the others because of their faster rotation period (as discussed above in Figure 8), so this is not a cut through the peak of the distribution at this energy.

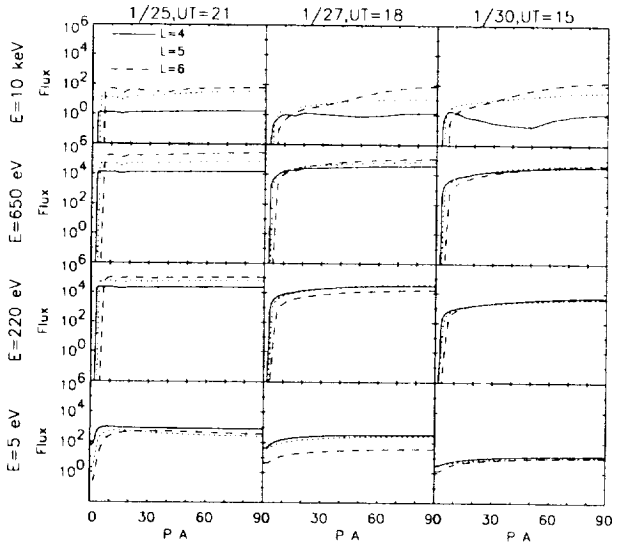

Figure 12. Local midnight plasma sheet electron pitch angle distributions at various energies and simulations times for late January 1991, shown at L=4 (solid line), 5 (dotted line), and 6 (dashed line).

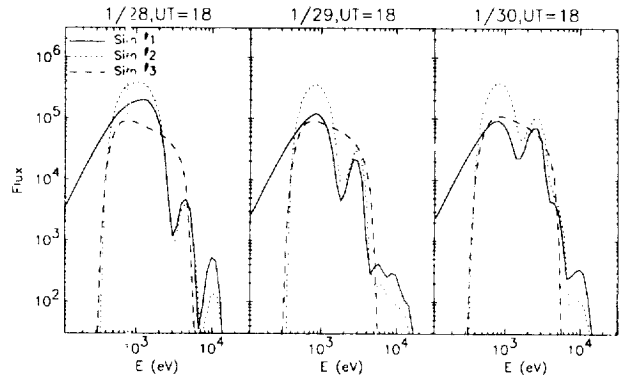

Figure 13. Comparison of plasma sheet electron energy spectra at L=4, MLT=0000 for three different simulations at various times. All three have the real Kp history, but Sim 1 has all processes included, Sim 2 has no Coulomb collisions, and Sim 3 has no Coulomb collisions or gradient-curvature drift (dashed line).

The pitch angle distribution of the injected PSEs is shown in Figure 12. Note that the injected distribution was isotropic in the trapped zone, and these results indicate that it remains quite isotropic throughout the simulation in both space and time. The only variation from isotropy is at high energies after several days of rotation. This is due to the pitch angle dependence of the gradient-curvature drift. The pitch angle distribution near the peak of the low-energy band shows signs of degradation after several days of rotation, and the fluxes near the loss cone are about an order of magnitude lower than at 90°.

5.3. Analysis of Plasma Sheet Electron Transport

Some analysis has already been discussed, but here a comparison of the results from the previous section with other simulations is presented. Figure 13 shows a comparison at L=4 and MLT=00 of three simulations at several times. The simulations are described in Table 4. All three have the same Kp history, but they have different combinations of included processes. Here it is seen that Coulomb collisions form the low-energy tail of the captured cloud. Without Coulomb collisions (Sim 2) there are no electrons below 200 eV at this spatial location due to the Fermi acceleration experienced during the Earthward convection. This low-energy tail forms at the expense of the peak intensity level of the lowest energy band. This is particularly evident in the last subplot, as the low-energy peak is not degrading in time or space. Coulomb scattering of electrons at energies of a few hundred eV has a timescale

Table 4. PSE Comparison Simulations

Simulation	Description
1	real Kp, all processes
2	real Kp, no Coulomb collisions
3	real Kp, no CC or G-C drifts
4	real up to t=48 then Kp=1, all processes
5	Kp=6 always, all processes

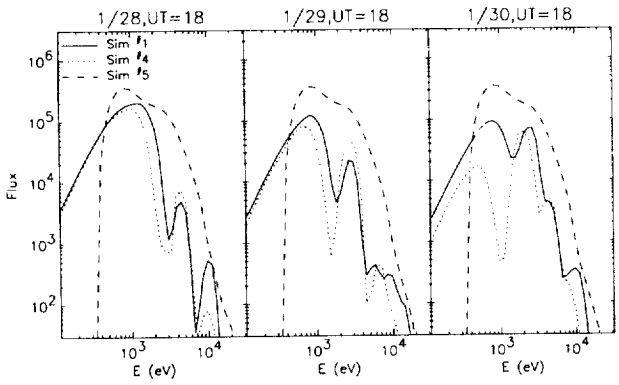

Figure 14. Comparison of plasma sheet electron energy spectra at L=4, MLT=0000 for three different Kp history simulations at various times. All three include all processes, but Sim 1 used the real Kp history, Sim 4 used the real Kp history through 1/26 and then switched to constant Kp=1, and Sim 5 used constant Kp=6.

of days [*Liemohn et al.*, 1997a, b], and the slow diffusion of particles into the loss cone is responsible for the slight degradation of the peak seen in Figure 11. With the removal of magnetic gradient-curvature drift as well, there is no banded structure formation at all, and Sim 3 simply shows an accelerated kappa distribution. The cloud is still captured in this simulation, but there is no degradation or distortion of the fluxes.

Figure 14 shows a comparison of Sim 1 with two more cases. Here, the three cases have all processes included but have different Kp histories. Sim 4 is the case without the third Kp spike, so all of the captured electrons are from the first two spikes. It is clear that this final Kp pulse only adds to the existing cloud and is not the sole source of the captured electrons, at least for the chosen boundary distribution. The differences between Sim 1 and Sim 4 in the last subplot is mainly due to differences in the thermal plasma due to the differing Kp histories. Sim 5, however, is completely different. The constantly high activity level pushes in the kappa distribution, and then constantly replenishes it. This is different from Sim 2 in that these particles are freshly injected instead of captured and undamped. There is no capture in Sim 5 because the activity is constant; a relaxation is necessary to capture a cloud of PSEs.

6. Combined Electron Distribution Function

The combination of the two sources described above gives new insight into the development of the total superthermal electron distribution in the inner magnetosphere. Also, a new feature of this model is the ability to calculate the low energy range of the superthermal electron distribution with a bounce-averaged technique, allowing for an accurate calculation of the energy deposition to the thermal plasma on a global scale. These two features will be discussed in this section.

6.1. Heating the Thermal Plasma

When energetic plasma is streaming through a background thermal plasma, the energetic particles will lose energy to the thermal plasma through Coulomb collisions. This results in an energy deposition from the energetic particles to the low-energy populations. The instantaneous volume heating rate Q is derived by integrating the Fokker-Planck collision term of Coulomb interactions over velocity space, and is a function of the superthermal electron omnidirectional flux and the thermal plasma density. Of particular interest is the heat flux into the ionosphere $P_\mathcal{E}$, obtained by integrating Q along the field line from the ionospheric footpoint to the equatorial plane [*Liemohn and Khazanov*, 1995]. This represents the energy flux into the ionospheric thermal population from the energetic population. Studies have shown that variations in $P_\mathcal{E}$ have great effects on the thermal, compositional, and optical structures in the ionosphere [*Chandler et al.*, 1988; *Kozyra et al.*, 1990; *Comfort et al.*, 1995].

Integrated thermal electron heating rates are shown in Plate 1 (it is a straightforward calculation to produce results for the other thermal plasma species as well). The five columns are defined as follows: heating from PEs; heating from PSEs; summed PE and PSE heating (sum of the first two columns); summed PE and PSE heating with 5 times the PSE density at the boundary as in the previous two columns (so n_{PSE}=0.5 cm^{-3} in the boundary kappa distribution); and summed PE and PSE heating with n_{PSE}=3.0 cm^{-3} at the boundary (30 times larger). This increase in density is simply a multiplier because of the linearity of (1) and (2), assuming that the injected distribution is held constant throughout the simulation. These last two columns are shown to represent injection from a dense plasma sheet [*Birn et al.*, 1997; *Borovsky et al.*, 1997].

The first row shows heating after steady state flux levels have been reached with constant Kp=1. Notice the strong dayside heating from the PEs with just a narrow band of heating around the nightside near L=5. Heating from the PSEs is limited to a strip around the dawnside along the outer boundary. This heating from the plasma sheet is so much weaker than the PE heating, it hardly changes the dawn sector of the summed plots from that of the PE results. It is interesting to note that most of the nightside is insignificantly heated by superthermal electrons for this case.

The second row shows results for steady state superthermal electron fluxes after constant Kp=6. The PE heating is greatly diminished from the Kp=1 values, with essentially no PE heating on the nightside. By contrast, though, the PSE energy deposition has increased dramatically throughout the inner magnetosphere. Keep in mind that these values are proportional to the thermal plasma density, so the decrease at large radial distances is primarily due to decreases in this density. This is also true for the deposition in the afternoon sector from both populations. The dependence of $P_\mathcal{E}$ on the thermal electron temperature is negligible because the characteristic energy of the superthermal electrons is much greater than T_e.

The bottom three rows of Plate 1 are results using the Kp history during the CRRES banded structure observations in late January 1991. The third row is during the final injection of plasma sheet particles when the peak of the cloud is at local midnight, the fourth row is twelve hours later, and the final row is more than two days after this, chosen so the cloud peak is again at local midnight. In the third row, significant heating is seen around the nightside due to PEs, in fact in all three times the nightside heating is more than the steady-state heating when Kp is held at 1. This is mostly due to differences in the thermal plasma density between the two simulations. The PSE heating rates are less than the Kp=6 values, and are not so

close to the Earth, but are still substantial, particularly with a denser source population. Twelve hours later, the cloud is on the dayside and far less of an influence because the PE heating is so much stronger there. In the fifth row, the band is degrading but still significantly contributing to heating the thermal plasma on the nightside, and is certainly still more important than PEs in this region.

6.2. Flux Comparisons

The heating rates in the previous section describe the composite influence of the superthermal electrons on the thermal plasma. It is also interesting to examine the combined distribution function in the superthermal energy range to understand how these bulk influences are generated. This will be done for the January 1991 results. As seen above, the Kp=1 results have no PSEs in most of the simulation domain and the steady state Kp=6 case is somewhat unrealistic (shown as an extreme case). Therefore these results will concentrate on a comparison of the distributions of PEs and PSEs during the CRRES banded structure observations.

Figure 15 shows energy spectra for the two source populations at various spatial locations for the third row of Plate 1, during the final Kp spike and PSE capture. The spatial locations are chosen to be in the nightside peak of the cloud (first row) and the nightside PE band (second row), and two analogous points on the dayside. Also, two equatorial pitch angles are shown: 90° and the loss cone boundary (LCB). Row 1 clearly shows the PSE dominance of the distribution throughout the pitch angle range, with fluxes several orders of magnitude larger than the PE fluxes at this location. In the narrow PE band on the nightside, however, PEs dominate the low-energy range of the spectrum, even at 90°. On the dayside, however, the intersection shifts to higher energies because of the proximity of the PE source, reaching 400 eV near the LCB at L=4. In every case, however, the PSEs dominate the high-energy part of the spectrum, often with positive gradients in the distribution at the intersection and elsewhere. It can be seen that rotating the PSE results by 12 hours will make the energy of the PSE-PE intersection decrease in the dayside plots and will also make the PEs more comparable to the PSEs on the nightside. As time continues, the PSE fluxes will degrade (no more injections), allowing more of the PE distribution to dominate the combined flux function.

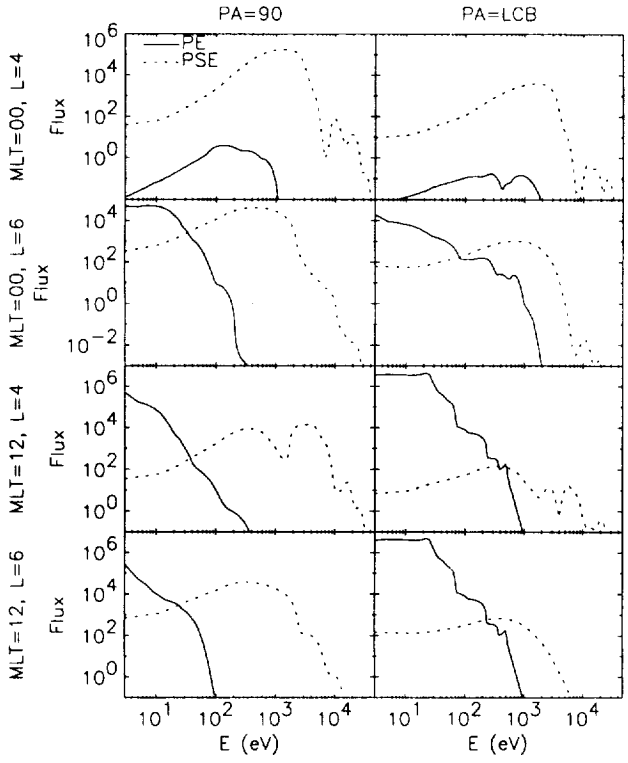

Figure 15. Energy spectra for photoelectrons (solid line) and plasma sheet electrons (dotted line) at various pitch angles and spatial locations on January 27, 1991, at UT=1800. This time corresponds to the third row of Plate 1.

The combined distribution function of superthermal electrons from these two sources is shown in Figure 16 throughout the CRRES observations at the 4 spatial locations discussed in Figure 15 (again at 90° and the LCB). Here the two populations have been summed into a single distribution. In the first column, PSEs form the nightside and PEs form the dayside distributions, except for the high-energy bulge at 90° at L=6. After this, the distribution becomes mixed, except in the first row, which is always dominated by PSEs. Notice the substantial number of spikes forming in the two L=4 rows at high energies. This is the banded structure forming inside of the Alfvén boundary after the capture of the PSEs, as the magnetic drifts cause the electrons at these energies to have a drift period shorter than the corotation period, and they eventually lap the low-energy electrons. This is not seen for most of the L=6 results because this is typically beyond the Alfvén boundary. Only after extended quiet times would this radial distance develop the banded structure seen closer in. Also notice that the pitch angle distributions always show a positive slope at the point of PE-PSE crossover. Furthermore, this slope is usually quite steep.

7. Discussion

By combining two time-dependent kinetic models of superthermal electron transport, a global calculation of the superthermal electron distribution function throughout the inner magnetosphere has been conducted. It has been shown that the energy range of validity for this combined model extended down to the superthermal-thermal intersection at a few eV (omitting transient field-aligned flows), allowing for the calculation of the entire distribution function and thus an accurate heating rate to the thermal plasma. Because of the linearity of the formulas, the source terms were separated to calculate the distributions from the various populations, namely photoelectrons (PEs) and plasma sheet electrons (PSEs). These distributions were recombined to show the development of the total superthermal electron distribution function.

It was shown that convection, corotation, and Coulomb collisions are the dominant processes in the formation of the PE distribution function. Because the source is the dayside ionosphere, a source cone exists in the magnetosphere that fills in the dayside trapped zone. These electrons then propagate around the nightside, experiencing depletion due to collisions with the thermal plasma and flux tube relaxation from magnetospheric convection. As a result, only a small band in L shell is still populated by PEs in the predawn sector, and this is mostly high-energy electrons in the trapped zone. This population creates a bulge in the PE distribution function on the morningside. Convection is also responsible for preventing the PEs from building up completely on the dayside because it sweeps away the particles from the trapped zone as

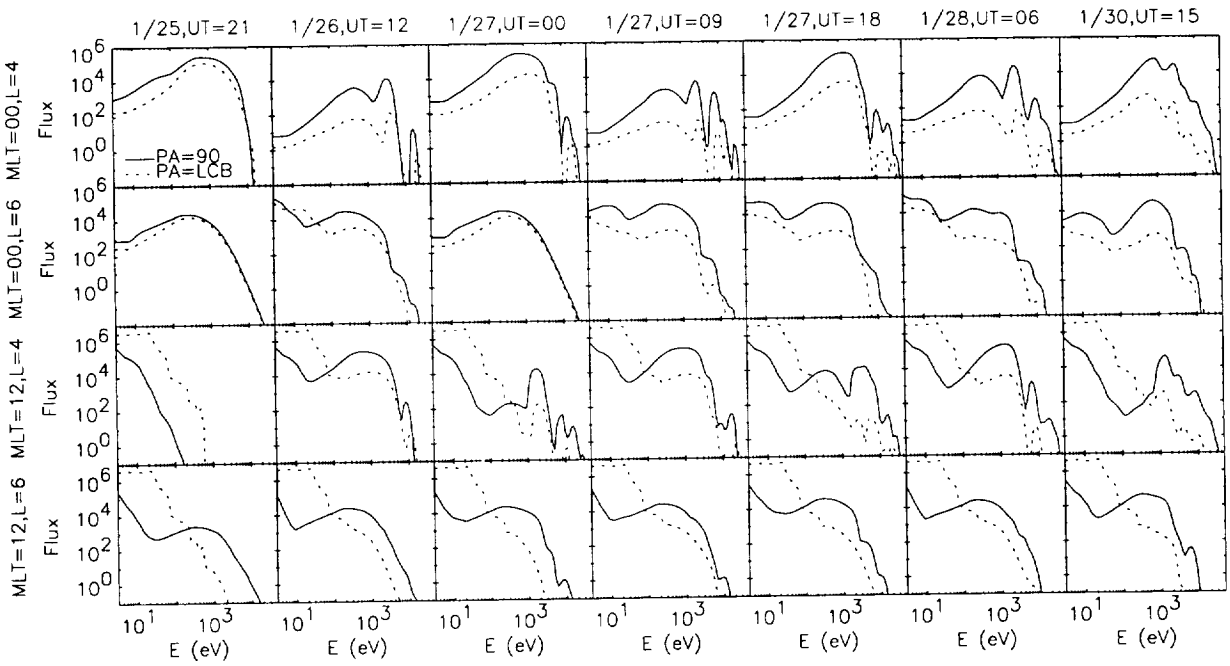

Figure 16. Time development of the combined-source superthermal electron distribution function at several spatial locations and pitch angles.

they are scattering in from the source cone. This effect is relatively small during quiet times, but becomes a dominant influence on the distribution function formation during disturbed conditions. It was shown that magnetic gradient-curvature drifts have essentially no effect on PEs because they are too low in energy to have a significant magnetic drift.

PSEs are dominated by the interplay between the drift terms. Coulomb collisions only contribute to the formation of the low-energy range of the distribution, and most of the high-energy portion is not greatly affected by these interactions. Under steady geomagnetic conditions, a flow pattern forms that prevents the PSEs from existing for long periods in the inner magnetosphere. When the activity increases, PSEs push closer in toward the Earth. When the activity subsequently relaxes, the PSEs closest to the Earth are then captured inside the Alfvén boundary, where they will rotate and remain for several days. Magnetic drifts cause the high-energy electrons to supercorotate, eventually lapping the lower-energy electrons and forming a banded structure in the energy spectra.

The combination of these two distributions shows that PEs supply a low-energy population to the distribution function, but that PSEs dominate the high-energy part of the distribution function, particularly at large pitch angles. On the dayside, there is a change from a source cone distribution to a loss cone distribution as energy increases above the PE range. On the nightside, however, the fluxes at small pitch angles are rarely larger than those deep in the trapped zone. It is concluded that the addition of PEs does not greatly alter the nightside mean energy of the captured PSE cloud observed by the CRRES satellite. Because PEs exist in such a narrow radial band in the nightside, this cannot account for the less-than-adiabatic increase of $T_\perp$ calculated from the lowest energy band observed by CRRES. Other mechanisms must be investigated to fully understand this phenomenon.

A distinctive feature of most of the simulations presented in this study is an absence of superthermal electrons inside of about L=3 on the nightside, prohibited by Coulomb losses (PEs) or corotation (PSEs). Only during prolonged periods of high geomagnetic activity can PSEs reach these L shells, and even then heating in this region is usually much less than on the dayside. An analysis of observed thermal plasma temperatures in this region for this effect is beyond the scope of this study, however. Conversely, these results show that PEs pump a substantial amount of energy into the thermal plasma on the dayside, particularly in the afternoon sector. These energy fluxes into the ionosphere typically approach 10^{10} eVcm^{-2}s^{-1} in the plasmaspheric region, dropping to 10^{8} and less outside the plasmapause. The PSEs, however, usually do not provide more than 10^{8} eVcm^{-2}s^{-1} to the thermal electrons for the chosen boundary conditions.

Note that while the combined model is capable of calculating the precipitation effects of superthermal electrons into the ionosphere, this study did not include this process for the sake of brevity and clarity. However, it is expected that the inclusion of this population will substantially enhance the energy deposition rate from the PSEs because these secondary electrons will have a much lower mean energy and therefore more efficiently heat the thermal plasma. It is also expected that this population will increase the extent of nightside heating from the PEs.

Another result from these combined spectra is that the distribution often has positive slopes with energy or pitch angle, indicating that instabilities could arise. Because the present study has focused on global convection along and across field lines, an analysis of the stability of these distributions has not been conducted here. This will be the topic of a later study, including the feedback from internally-generated waves and the influences of externally-imposed waves.

Acknowledgments. This work was supported by the National Science Foundation under contracts ATM-9710326, ATM-9896049, ATM-9800830, and NASA contract NAG5-

6976. MWL worked under a National Research Council Postdoctoral Associateship at NASA MSFC. Work at GSFC was supported by the NASA Research and Analysis Program under UPN 310-10-16.

The Editor thanks R. Link and another referee for their assistance in evaluating this paper.

References

Alfvén, H., and C.-G. Fälthammar, *Cosmical Electrodynamics*, Oxford Univ. Press, Oxford, 1963.

Arnoldy, R. L., Fine structure and pitch angle dependence of synchronous orbit electron injections, *J. Geophys. Res., 91*, 13,411, 1986.

Arnoldy, R. L., and T. E. Moore, Longitudinal structure of substorm injections at synchronous orbit, *J. Geophys. Res., 88*, 6213, 1983.

Avakyan, S. V., M. N. Vlasov, and I. A. Krinberg, comparison of the fluxes and spectra of Auger electrons and photoelectrons in the Earth's ionosphere and plasmasphere, *Geomagn. Aeron., 17*, 54, 1977.

Banks, P. M., and A. F. Nagy, Concerning the influence of elastic scattering upon photoelectron transport and escape, *J. Geophys. Res., 75*, 1902, 1970.

Barfield, J. N., S. E. DeForest, and D. J. Williams, Simultaneous observations of substorm electrons: Explorer 45 and ATS 5, *J. Geophys. Res., 82*, 531, 1977

Baumjohann, W., G. Paschmann, and C. A. Cattell, Average plasma properties in the central plasma sheet, *J. Geophys. Res., 94*, 6597, 1989.

Berger, M. J., S. M. Seltzer, and K. Maeda, Some new results on electron transport in the atmosphere, *J. Atmos. Terr. Phys., 32*, 1015, 1970.

Birn, J., M. F. Thomsen, J. E. Borovsky, G. D. Reeves, D. J. McComas, and R. D. Belian, Characteristic plasma properties during dispersionless substorm injections at geosynchronous orbit, *J. Geophys. Res., 102*, 2309, 1997.

Borovsky, J. E., M. F. Thomsen, and D. J. McComas, The superdense plasma sheet: Plasmaspheric origin, solar wind origin, or ionospheric origin?, *J. Geophys. Res., 102*, 22,089, 1997.

Burke, W. J., A. G. Rubin, D. A. Hardy, and E. G. Holeman, Banded electron structures in the plasmasphere, *J. Geophys. Res., 100*, 7759, 1995.

Butvin, G. G., G. V. Popov, and G. V. Khazanov, Possible instability of primary photoelectron streams, *Cosmic Res., 13*, 545, 1975.

Chandler, M. O., J. U. Kozyra, J. L. Horwitz, R. H. Comfort, and L. H. Brace, Modeling of the thermal plasma in the outer plasmasphere -- A magnetospheric heat source, in *Modeling Magnetospheric Plasma, Geophys. Monogr. Ser.*, vol. 44, edited by T. E. Moore and J. H. Waite Jr., p. 101, AGU, Washington, D. C., 1988.

Christon, S. P., D. J. Williams, D. G. Mitchell, L. A. Frank, and C. Y. Huang, Spectral characteristics of plasma sheet ion and electron populations during undisturbed geomagnetic conditions, *J. Geophys. Res., 94*, 13,409, 1989.

Cicerone, R. J., and S. A. Bowhill, Photoelectron fluxes in the ionosphere computed by a Monte Carlo method, *J. Geophys. Res., 76*, 8299, 1971.

Comfort, R. H., P. G. Richards, P. D. Craven, and M. O. Chandler, Problems in simulating ion temperatures in low density flux tubes, in *Cross-Scale Coupling in Space Plasmas, Geophys. Monogr. Ser.*, vol. 93, edited by J. L. Horwitz, N. Singh, and J. L. Burch, p. 155, AGU, Washington, D. C., 1995.

DeForest, S. E., and C. E. McIlwain, Plasma clouds in the magnetosphere, *J. Geophys. Res., 76*, 3587, 1971.

Doering, J. P., W. K. Peterson, C. O. Bostrom, and T. A. Potemra, High resolution daytime photoelectron energy spectra from AE-E, *Geophys. Res. Lett., 3*, 129, 1976.

Eather, R. H., S. B. Mende, and R. J. R. Judge, Plasma injection at synchronous orbit and spatial and temporal auroral morphology, *J. Geophys. Res., 81*, 2805, 1976.

Ejiri, M., Trajectory traces of charged particles in the magnetosphere, *J. Geophys. Res., 83*, 4798, 1978.

Ejiri, M., R. A. Hoffman, and P. H. Smith, The convection electric field model for the magnetosphere based on Explorer 45 observations, *J. Geophys. Res., 83*, 4811, 1978.

Ejiri, M., R. A. Hoffman, and P. H. Smith, Energetic particle penetrations into the inner magnetosphere, *J. Geophys. Res., 85*, 653, 1980.

Evans, D. S., and T. E. Moore, Precipitating electrons associated with the diffuse aurora: Evidence for electrons of atmospheric origin in the plasma sheet, *J. Geophys. Res., 84*, 6451, 1979.

Fok, M.-C., Decay of ring current ions and associated aeronomical consequences, Ph.D. thesis, Univ. of Mich., Ann Arbor, 1993.

Fok, M.-C., J. U. Kozyra, A. F. Nagy, C. E. Rasmussen, and G. V. Khazanov, A decay model of equatorial ring current and the associated aeronomical consequences, *J. Geophys. Res., 98*, 19,381, 1993.

Galperin, Y. I., and T. M. Mulyarchik, On the height distribution of photoelectrons, *Cosmic Res., 4*, 932, 1966.

Guiter, S. M., T. I. Gombosi, and C. E. Rasmussen, Two-stream modeling of plasmaspheric refilling, *J. Geophys. Res., 100*, 9519, 1995.

Hinton, F. L., Collisional transport in plasma, in *Handbook of Plasma Physics*, vol. 1, *Basic Plasma Physics I*, edited by A. A. Galeev and R. N. Sudan, p. 147, North-Holland, New York, 1983.

Huang, C. Y., and L. A. Frank, A statistical study of the central plasma sheet: Implications for substorm models, *Geophys. Res. Lett., 13*, 652, 1986.

Hultqvist, B., B. Aparicio, H. Borg, R. Arnoldy, and T. E. Moore, Decrease of keV electron and ion fluxes in the dayside magnetosphere during the early phase of magnetospheric disturbances, *Planet. Space Sci. 29*, 107, 1981.

Ivanov, V. B., Trukhan, A. A., and G. V. Khazanov, Stability of the mid-latitude ionospheric plasma in the presence of photoelectrons, *Radiofizika, 23*, 43,1980.

Ivanov, V. B., A. A. Trukhan, and G. V. Khazanov, Mid-latitude F-region ionosphere plasma instability in the presence of photoelectrons, *Ann. Geophys. 38*, 33, 1982.

Jasperse, J. R., Boltzmann-Fokker-Planck model for the electron distribution function in the earth's ionosphere, *Planet. Space Sci., 24*, 33, 1976.

Jasperse, J. R., and E. R. Smith, The photoelectron flux in the Earth's ionosphere at energies in the vicinity of photoionization peaks, *Geophys. Res. Lett., 5*, 843, 1978.

Jordanova, V. K., Kinetic modeling of the terrestrial ring current, Ph.D. thesis, Univ. of Mich., Ann Arbor, 1995.

Jordanova, V. K., L. M. Kistler, J. U. Kozyra, G. V. Khazanov, and A. F. Nagy, Collisional losses of ring current ions, *J. Geophys. Res., 101*, 111, 1996.

Kaye, S. M., and M. G. Kivelson, Time dependent convection electric fields and plasma injection, *J. Geophys. Res., 84*, 483, 1979.

Kerns, K. J., D. A. Hardy, and M. S. Gussenhoven, Modeling of convection boundaries seen by CRRES in 120-eV to 28-keV particles, *J. Geophys. Res., 99*, 2403, 1994.

Khazanov, G. V., and G. D. Gefan, The kinetics of ionosphere-plasmasphere transport of superthermal electrons, *Phys. Solariterr., 19*, 65, 1982.

Khazanov, G. V., and M. W. Liemohn, Non-steady-state ionosphere-plasmasphere coupling of superthermal electrons, *J. Geophys. Res., 100*, 9669, 1995.

Khazanov, G. V., and M. W. Liemohn, Comparison of photoelectron theory against observations, in *Geophysical Monograph Series*, edited by J. L. Horwitz, AGU, Washington, D. C., in press, 1998.

Khazanov, G. V., M. A. Koen, and S. I. Burenkov, Kinetic equation for photoelectrons in the plasmasphere averaged over oscillations between reflection points, *Cosmic Res., 17*, 385, 1979a.

Khazanov, G. V., M. A. Koen, and S. I. Burenkov, A numerical solution to the kinetic equation for photoelectrons taking into account the free and trapped zones, *Cosmic Res., 17*, 741, 1979b.

Khazanov, G. V., T. I. Gombosi, A. F. Nagy, and M. A. Koen, Analysis of the ionosphere-plasmasphere transport of superthermal electrons, 1, Transport in the plasmasphere, *J. Geophys. Res., 97*, 16887, 1992.

Khazanov, G. V., M. W. Liemohn, T. I. Gombosi, and A. F. Nagy, Non-steady-state transport of superthermal electrons in the plasmasphere, *Geophys. Res. Lett., 20*, 2821, 1993.

Khazanov, G. V., T. Neubert, and G. D. Gefan, Kinetic theory of ionosphere plasmasphere transport of suprathermal electrons, *IEEE Trans. Plasma Sci., 22*, 187, 1994.

Khazanov, G. V., T. E. Moore, M. W. Liemohn, V. K. Jordanova, and M.-C. Fok, Global, collisional model of high-energy photoelectrons, *Geophys. Res. Lett., 23*, 331, 1996.

Koons, H. C., and J. F. Fennell, Particle and wave dynamics during plasma injections, *J. Geophys. Res., 88*, 6221, 1983.

Kozyra, J. U., C. E. Valladares, H. C. Carlson, M. J. Buonsanto, and D. W. Slater, A theoretical study of seasonal and solar cycle variations of stable aurora red arcs, *J. Geophys. Res., 95*, 12219, 1990.

Kudryashev, G. S., A. A. Trukhan, and G. V. Khazanov, Fine structure of photoelectron spectra, *Cosmic Res., 17*, 521, 1979.

Lejeune, G., "Two stream" photoelectron distributions with interhemispheric coupling: A mixing of analytical and numerical methods, *Planet. Space Sci., 27*, 561, 1979.

Lejeune, J., and F. Wörmser, Diffusion of photoelectrons along a field line inside the plasmasphere, *J. Geophys. Res., 81*, 2900, 1976.

Leveque, R. J., *Numerical Methods for Conservation Laws*, 2nd ed., Birkhäuser Verlag, Boston, Mass., 1992.

Liemohn, M. W., and G. V. Khazanov, Non-steady-state coupling processes in superthermal electron transport, in *Cross-Scale Coupling in Space Plasmas, Geophys. Monogr. Ser.*, vol. 93, edited by J. L. Horwitz, N. Singh, and J. L. Burch, p. 181, AGU, Washington, D. C., 1995.

Liemohn, M. W., and G. V. Khazanov, Determining the significance of electrodynamic coupling between superthermal electrons and thermal plasma, in *Geophysical Monograph Series*, edited J. L. Horwitz, AGU, Washington, D. C., in press, 1998.

Liemohn, M. W., G. V. Khazanov, T. E. Moore, and S. M. Guiter, Self-consistent superthermal electron effects on plasmaspheric refilling, *J. Geophys. Res., 102*, 7523, 1997a.

Liemohn, M. W., G. V. Khazanov, and J. U. Kozyra, Guided plasmaspheric hiss interactions with superthermal electrons, 1, Resonance curves and timescales, *J. Geophys. Res., 102*, 11,619, 1997b.

Liemohn, M. W., G. V. Khazanov, and J. U. Kozyra, Banded electron structure formation in the inner magnetosphere, *Geophys. Res. Lett., 25*, 877, 1998.

Link, R., Feautrier solution of the electron transport equation, *J. Geophys. Res., 97*, 159, 1992.

Lummerzheim, D., M. N. Rees, and H. R. Anderson, Angular dependent transport of auroral electrons in the upper atmosphere, *Planet. Space Sci., 37*, 109, 1989.

Mantas, G. P., and S. A. Bowhill, Calculated photoelectron pitch-angle and energy spectra, *Planet. Space Sci., 23*, 355, 1975.

Mantas, G. P., H. C. Carlson, and V. B. Wickwar, Photoelectron flux buildup in the plasmasphere, *J. Geophys. Res., 83*, 1, 1978.

Maynard, N. C., and A. J. Chen, Isolated cold plasma regions: Observations and their relation to possible production mechanisms, *J. Geophys. Res., 80*, 1009, 1975.

McComas, D. J., S. J. Bame, B. L. Barraclough, J. R. Donart, R. C. Elphic, J. T. Gosling, M. B. Moldwin, K. R. Moore, and M. F. Thomsen, Magnetospheric plasma analyzer: Initial three-spacecraft observations from geosynchronous orbit, *J. Geophys. Res., 98*, 13,453, 1993.

McGuire, T., and M. Liemohn, Performance of a bounce-averaged global model of superthermal electron transport in the Earth's magnetic field, in *NASA/ASEE Sum. Fac. Fell. Prog. 1997 Rept.*, 33-1, 1997.

Moore, T. E., and R. L. Arnoldy, Plasma pitch angle distributions near the substorm injection front, *J. Geophys. Res., 87*, 265, 1982.

Moore, T. E., R. L. Arnoldy, J. Feynmann, and D. A. Hardy, Propagating substorm injection fronts, *J. Geophys. Res., 86*, 6713, 1981.

Nagy, A. F., and P. M. Banks, Photoelectron fluxes in the ionosphere, *J. Geophys. Res., 75*, 6260, 1970.

Peterson, W. K., J. P. Doering, T. A. Potemra, R. W. McEntire, and C. O. Bostrom, Conjugate photoelectron fluxes observed on Atmospheric Explorer C, *Geophys. Res. Lett.,4*, 109, 1977.

Polyakov, V. M., G. V. Khazanov, and M. A. Koen, Mathematical model of photoelectron fluxes in the mid-latitude ionosphere, *Cosmic Res., 14*, 543, 1976.

Polyakov, V. M., G. V. Khazanov, and M. A. Koen, The ionosphere-plasmasphere photoelectron transport, *Phys. Solariterr., 10*, 93, 1979.

Porter, H. S., F. Varosi, and H. G. Mayr, Iterative solution of the multi-stream electron transport equation, 1, Comparison with laboratory beam injection experiments, *J. Geophys. Res., 92*, 5933, 1987.

Prather, M. J., M. B. McElroy, and J. Rodriguez, Photoelectrons in the upper atmosphere: A formulation incorporating effects of transport, *Planet. Space Sci., 26*, 131, 1978.

Rasmussen, C. E., S. M. Guiter, and S. G. Thomas, Two-dimensional model of the plasmasphere: Refilling time constants, *Planet. Space Sci., 41*, 35, 1993.

Roederer, J. G., *Dynamics of Geomagnetically Trapped Radiation*, Springer-Verlag, New York, 1970.

Sanatani, S., and W. B. Hanson, Plasma temperature in the magnetosphere, *J. Geophys. Res., 75*, 769, 1970.

Solomon, S. C., Auroral electron transport using the Monte Carlo method, *Geophys. Res. Lett., 20*, 185, 1993.

Stamnes, K., Analytic approach to auroral electron transport and energy degradation, *Planet. Space Sci.*, 28, 427, 1980.

Stern, D. P., The motion of a proton in the equatorial magnetosphere, *J. Geophys. Res., 80*, 595, 1975.

Strickland, D. J., D. L. Book, T. P. Coffey, and J. A. Fedder, Transport equation techniques for the deposition of auroral electrons, *J. Geophys. Res., 81*, 2755, 1976.

Swartz, W. E., G. J. Bailey, and R. J. Moffett, Electron heating resulting from interhemispherical transport of photoelectrons, *Planet. Space Sci., 23*, 589, 1975.

Takahashi, T., Energy degradation and transport of photoelectrons escaping from the upper ionosphere. *Rept. Ionos. Space Res. Jpn., 27* (1), 79, 1973.

Victor, G. A., K. Kirby-Docken, and A. Dalgarno, Calculations of the equilibrium photoelectron flux in the thermosphere, *Planet. Space Sci., 24*, 679, 1976.

Volland, H., A semiempirical model of large-scale magnetospheric electric fields, *J. Geophys. Res., 78*, 171, 1973.

Winningham, J. D., D. T. Decker, J. U. Kozyra, J. R. Jasperse, and A. F. Nagy, Energetic (>60 eV) atmospheric photoelectrons, *J. Geophys. Res., 94*, 15,335, 1989.

G. V. Khazanov, Geophysical Institute, University of Alaska, Fairbanks, AK 99775-7320. (khazanov@gi.alaska.edu)

J. U. Kozyra, Space Physics Research Laboratory, University of Michigan, Ann Arbor, MI 48109.

M. W. Liemohn, Space Sciences Laboratory, NASA Marshall Space Flight Center, Huntsville, AL 35812.

T. E. Moore, Laboratory for Extraterrestrial Physics, NASA Goddard Space Flight Center, Greenbelt, MD 20771.

(Received March 25, 1998; revised June 29, 1998;
accepted June 30, 1998.)